New constraints on the chemical composition and outgassing of 67P/Churyumov-Gerasimenko

C. Herny, O. Mousis, R. Marschall, N. Thomas, M. Rubin, O. Pinzón-Rodríguez, I.P. P Wright

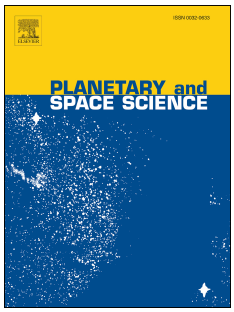

New constraints on the chemical composition and outgassing of 67P/Churyumov-Gerasimenko

C. Herny, O. Mousis, R. Marschall, N. Thomas, M. Rubin, O. Pinzón-Rodríguez, I.P. Wright

PII: S0032-0633(21)00033-7

DOI: https://doi.org/10.1016/j.pss.2021.105194

Reference: PSS 105194

To appear in: *Planetary and Space Science*

Received Date: 24 April 2020

Revised Date: 25 January 2021

Accepted Date: 25 February 2021

Please cite this article as: Herny, C., Mousis, O., Marschall, R., Thomas, N., Rubin, M., Pinzón-Rodríguez, O., Wright, I.P., New constraints on the chemical composition and outgassing of 67P/Churyumov-Gerasimenko, *Planetary and Space Science*, https://doi.org/10.1016/j.pss.2021.105194.

Clémence Herny: Conceptualization, Software, Validation, Formal analysis, Writing - Original Draft, Visualization. **Olivier Mousis:** Conceptualization, Supervision, Resources, Writing - Review & Editing. **Raphael Marschall:** Conceptualization, Resources, Writing - Review & Editing. **Nicolas Thomas:** Conceptualization, Resources, Supervision, Writing - Review & Editing. **Martin Rubin:** Resources, Writing - Review & Editing. **Olga Pinzón-Rodríguez:** Writing - Review & Editing. **Ian P. Wright:** Writing - Review & Editing.

New constraints on the chemical composition and outgassing of 67P/Churyumov-Gerasimenko

C. Herny[a,*], O. Mousis[b], R. Marschall[c], N. Thomas[a], M. Rubin[a], O. Pinzón-Rodríguez[a], I. P. Wright[d]

[a] Physikalisches Institut, Universität Bern, Sidlerstrasse 5, 3012 Bern, Switzerland

[b] Aix Marseille Université, CNRS, LAM (Laboratoire d'Astrophysique de Marseille) UMR 7326, F-13388, Marseille, France

[c] Southwest Research Institute, 1050 Walnut St., Boulder, CO 80302, USA

[d] Open University, School of Physical Sciences, Walton Hall, Milton Keynes MK7 6AA, Bucks, England

* Corresponding author: clemence.herny@space.unibe.ch

Abstract

Strong heterogeneities in the composition of the volatile species have been detected in the coma of comet 67P/Churyumov-Gerasimenko (67P/C-G) by the ROSINA instrument onboard the ESA's Rosetta spacecraft. However, it is not clear if these heterogeneities are indicative of heterogeneities in the near-surface nucleus composition or if the coma composition is mainly insolation-driven. In order to clarify the link between the composition of the nucleus and the composition of the coma we have performed numerical simulations and compare our results with measurements acquired by ROSINA/DFMS for three major volatile species namely, H_2O, CO_2, and CO. We use a previously published thermo-physical numerical model designed to study cometary nucleus evolution, including volatile outgassing and internal stratigraphy, as the comet orbits the Sun. The model follows schemes used for much of the past three decades to model cometary outgassing. Our results match well the experimental volatiles density measurements of ROSINA/DFMS for most of the Rosetta mission. They suggest that the outgassing pattern is mainly insolation-driven and the variations are caused by the tilt of rotation axis and eccentricity of the nucleus. The nucleus shows to

1st order a homogeneous composition and therefore we can provide constraints on the bulk volatiles composition of 67P/C-G nucleus which is dominated by H_2O (91.4% ± 4.5%), then CO_2 (6.7% ± 3.5%) and CO in small amount (1.9% ± 1.2%). However, in details, a dichotomy in composition between the northern and southern hemispheres of the comet is revealed. A CO/CO_2 bulk composition ratio of about 0.6 ± 0.1 is required to reproduce the measurements from the northern hemisphere and about 0.2 ± 0.1 for the southern hemisphere. To match the data, the thermal properties of the nucleus surface must be modified by adding a thin desiccated dust mantle (~5 mm) for northern latitudes while this appears not to be necessary for southern latitudes. This may be related to the observed dichotomy in putative airfall deposits. We suspect that, because of thermal inertia, seasonally non-illuminated areas continue to outgas and influence the ROSINA measurements. This effect cannot be reproduced with the model. Therefore during some periods of the mission, the fits are not ideal. Finally, the outgassing of the different ices leads to a layered internal structure defined by the sublimation front of each ice and formation of harder layers close to the surface due to sublimation/condensation processes. However, the thermo-physical model overestimates the absolute volatiles production (mainly in the southern hemisphere) leading to an overestimation of the erosion rates. Further investigations will be performed to improve the thermo-physical model and the sensitivity analysis.

Keywords: comet 67P/Churyumov-Gerasimenko; comet composition and internal structure; volatiles outgassing; thermal modelling of cometary nucleus; ROSINA/DFMS data

1. Introduction

Comets are thought to have retained a pristine internal structure since the formation of the Solar System. Therefore studying their composition and internal structure may provide constraints on conditions present in the protoplanetary disk. But determining their composition and internal structure is challenging because, following the problems with the Philae lander (Boehnhardt et al. 2017), our main sources of information were acquired remotely. We can get an idea of the species present in cometary nuclei by analysing the gas emitted from the surface into the coma. Although instruments

detect heterogeneity in the abundances of species in the coma of different comets (Krankowsky et al. 1986, Feaga et al., 2007, A'Hearn et al., 2011, Hässig et al., 2015, Hoang et al., 2017, 2019), it is not clear that this indicates compositional heterogeneity of the nucleus itself (Hässig et al., 2015, Fink et al., 2016). The ROSINA/DFMS mass spectrometer (Balsiger et al., 2007) on board the European Space Agency's Rosetta spacecraft has measured the density of various species at the location of the spacecraft inside the coma of comet 67P/Churyumov-Gerasimenko (hereafter 67P/C-G). Results display strong variations of the relative abundances of major volatiles in the coma (Hässig et al., 2015). Several studies proposed that the complex shape of the nucleus and the large tilt of the rotation axis of 67P/C-G of 52° (Sierks et al., 2015, Brugger et al. 2016) would imply large daily and seasonal effects driving the species outgassing (De Sanctis et al., 2010, Fougere et al., 2016, Fink et al., 2016, Fulle et al., 2016b) while others suggest that the diversity of surface morphologies of 67P/C-G results from non-uniform sub-surface composition (Vincent et al., 2015; Mousis et al., 2015, Keller et al., 2017). While previous studies of comets from fly-bys and ground-based observations have been thorough, even the detailed observations of 67P/C-G by the Rosetta spacecraft have failed to provide a clear answer to the question of whether comets are predominantly homogeneous in composition or not (Hässig et al., 2015).

The present study attempts to address this complicated issue by comparing the volatiles density measurements provided by the ROSINA/DFMS instrument with a thermo-physical numerical model based on the work of Marboeuf et al., (2008, 2012) designed to follow the evolution of a nucleus as it outgasses. Previous studies have provided estimates of the bulk composition of 67P/C-G using indirect methods (Rubin et al., 2019, Combi et al., 2020, Läuter et al., 2019, Bockelée-Morvan et al., 2016, Biver et al., 2019). With this direct approach, we can combine, for the first time, both the influence of the chemical composition and the physical properties of the nucleus to understand the complex relation between the outgassing nucleus and its resulting coma.

In the following section, we shall discuss the dataset to be modelled, the model itself and the applied boundary conditions. In Section 3, we shall present detailed comparisons of the model results with the data. In Section 4 we present insight on surface evolution and internal structure. Sections 5 and 6 provide the usual discussion and conclusions.

2. Data and method

a. Mass spectrometry measurements

The ROSINA (Rosetta Orbiter Spectrometer for Ion and Neutral Analysis) experiment (Balsiger et al., 2007) comprises three complementary instruments dedicated to monitor the composition, gas speed, and temperature of the neutral gas coma. Among this suite of instruments, we used the data acquired by the DFMS (Double Focusing Mass Spectrometer) which is a high resolution mass spectrometer. It acquired a mass spectrum during ~50 min from mass/charge 13 – 100 u/e in steps of 1 u/e providing the relative bulk composition (relative abundance) of the coma at the time of the measurement at the location of Rosetta. Using the pressure sensor COPS (COmetary Pressure Sensor) then allows obtaining absolute densities of the different species (Gasc et al. 2017, Rubin et al. 2019). The orbiting spacecraft explored different sub-spacecraft latitudes and longitudes of the comet throughout the measurement periods (Section 2.d, Fig. 4), however, it must be pointed out that gas may originate from any location within the field of view of ROSINA.

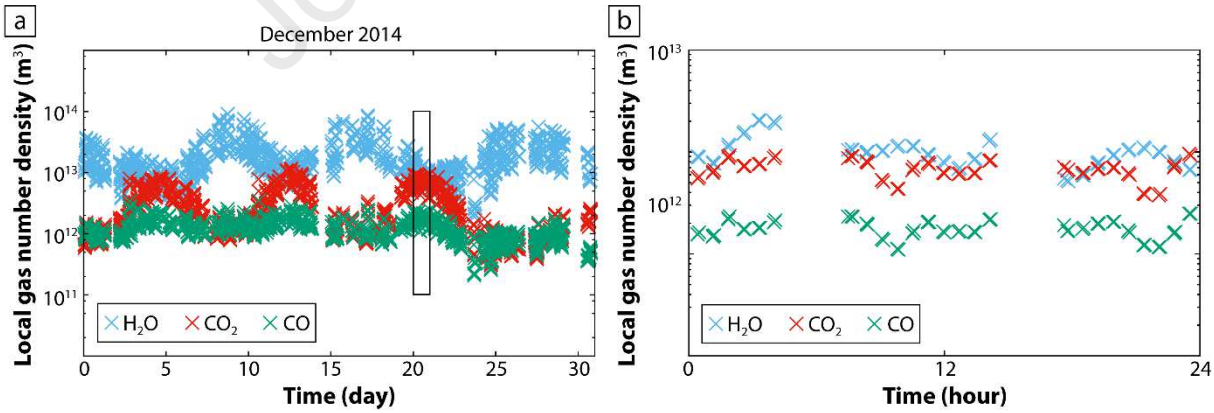

Fig. 1: (a) Local gas number density evolution of H_2O (blue crosses), CO_2 (red crosses), and CO (green crosses) measured by ROSINA on board Rosetta for the period of December 2014. (b) Detail from 20th December highlighted by the black box in (a).

In this study we focus on three of the major species detected in the coma: H_2O, CO_2 and CO (Fig. 1) (Le Roy et al., 2015; Hässig et al., 2015). Temporal and spatial variabilities of the coma composition have been detected (Hässig et al., 2015). It appears that sometimes the production of CO_2 and CO exceeds that of H_2O and that CO_2 and CO vary with respect to H_2O (Fig. 1, before equinox, Fougere et al., 2016). Errors in the ROSINA number density are dependent upon the combination of the two instruments COPS and DFMS. The error in the absolute density provided by COPS is <15% (Kramer et al. 2017) and the error in the relative abundances provided by DFMS is <30% (Rubin et al. 2019; Läuter et al. 2020).

b. The comet nucleus numerical model

The production rates of species coming out from the nucleus have been investigated via a numerical model. The model is based upon work carried out by Klinger in the 1990s (e.g. Klinger et al., 1996, Klinger, 1999) but the specific implementation is that of Marboeuf et al., (2008, 2012, 2014). We note that several other models of the evolution of cometary nuclei have been published and used in the past. A summary of many of these can be found in Huebner (2002).

The model was designed to compute the thermal and chemical evolution of the (sub)-surface of a single point at a given cometary latitude, λ, of the nucleus along the comet's orbit around the Sun (Fig. 2). The nucleus is considered to be a porous sphere made of a mixture of ices and dust grains defined in specified proportions. At the beginning of the simulation, ices and dust grains are homogeneously mixed in the porous matrix, up to the nucleus surface. The cometary grains are defined as spherical and compact refractory dust grains encased by volatile ices (Marboeuf et al., 2012). This assumption is consistent with one of the theory proposed to explain the aggregation of material in protoplanetary disks and comets (Greenberg et al., 1998, Huebner et al., 2006, Schoonenberg and Ormel, 2017, Mousis et al., 2018). The nucleus has an initially defined radius, R, and rotation period, T, around its rotation axis, Ω. The model computes, amongst other quantities, the heat conduction and evolution at different depths, the sublimation/condensation of volatiles within the nucleus, the gas diffusion through a porous medium and the sublimation front of different ices along

135 the comet's orbit around the Sun. The model can also take into account the presence of a dust mantle
136 at the surface.
137

138

139 **Fig. 2:** Principle of the numerical model. The comet is considered to be a spherical object with radius,
140 R. Outputs of the model are computed in 1D along the u_r vector for a given latitude λ while the comet
141 is rotating around its spin axis Ω and on its orbit around the Sun. The two points, A and P, correspond
142 to the aphelion and perihelion positions respectively.
143

144 The model solves the linked equations for conservation of energy and mass, described in detail
145 in Marboeuf et al. (2012). They are solved by the finite volume method, in spherical coordinates and
146 in one dimension, along the radial vector u_r (Fig. 2). Lateral processes are neglected. The gas diffuses
147 through the pores by a flow mechanism defined by the Knudsen number. Even if the comet is far from
148 a sphere (Preusker et al., 2015; Jorda el al., 2016), the spherical approximation is suitable to study a
149 single point that is not subject to shadowing by other surface facets. We note that areas on the surface
150 of 67P/C-G's nucleus experience significant shadowing affecting the energy input and therefore the
151 outgassing (Keller et al. 2015b). However, we aim to focus on the chemical composition and not bring
152 additional complexity to the already sophisticated thermo-physical model with a 3D complex shape
153 and illumination that will increase the computational times beyond what we can reasonably be
154 achieved. A 3D model taking into account of the physical and chemical aspects of the presented 1D
155 numerical model (Marboeuf et al. 2012, 2014) has not been developed so far. We can say, however,
156 that this simplification leads to an overestimation of the outgassing, a point that will be addressed in

section 2.d. The numerical domain takes into account the whole comet radius with the nucleus centre placed at z = 0 and surface at z = R. The surface temperature is computed with an energy balance equation and the centre temperature is set as a Neumann condition. The model uses a spatial discretization in a grid in which equations are computed for every numerical layer. The discretization comprises (1) a fixed number of layers with a minimum thickness, placed just below the surface to ensure good spatial resolution as most of the driving processes occur close to the surface (solar heating, sublimation of volatiles, evolution of the radius, dust mantle) because of the low thermal conductivity (Section 2.c) and then (2) an exponential increase of the layer thickness, for a given number of layers, from the sub-surface to the centre of the nucleus. The number of layers, and therefore their thicknesses, evolve as the sublimation/condensation of ices occurs. In effect, the code is solving Stefan's problem. The temporal discretization follows the corrector-predictor scheme developed by Espinasse et al. (1991) with the complementary use of an implicit scheme and a semi-implicit scheme avoiding instabilities and improving accuracy. Numerical tests have shown that results from the model have a high degree of confidence because the error in the mass conservation does not exceed 0.1% for the global error and 1% for the local error at a given time, t (Marboeuf, 2008).

c. Input parameters

Characteristic properties of 67P/C-G are used as inputs to the model and are presented in Table 1. The comet has an orbital period of 6.44 years with an aphelion at 5.68 AU and perihelion at 1.24 AU. The last perihelion occurred on 13 August 2015 (1.24 AU), the 1st equinox on 11 May 2015 (1.67 AU) and the 2nd equinox on 20 March 2016 (2.62 AU). At the time of the rendezvous of the Rosetta spacecraft with 67P/C-G, the period of rotation of the comet was about 12.40 h (Mottola et al., 2014). We acknowledge that the observed spin-up of the nucleus (Keller et al. 2015a, Accomazzo et al. 2017) could not be implemented in the model at this stage. The orientation of the spin axis with respect to the orbit is defined by (1) the obliquity Ω, which is about 52.25° (Jorda et al., 2016) and (2) the argument of the subsolar meridian at perihelion set at -110.50° (Brugger et al., 2016).

The initial temperature of the nucleus is set to 30 K (plausible temperature in the protoplanetary disk during comet formation (Yamamoto, 1985) and temperature derived from ortho-para ratio of water vapour in comets (Mumma et al. 1987)) and the radius of the comet is initially set to 2 km. This evolves as the comet approaches the Sun. The nucleus has a porosity of ~75% (Kofman et al., 2015, Pätzold et al., 2016; Taylor et al., 2017) with an averaged pore radius assumed to be of 10^{-4} m (Huebner, 2006). The dust-to-ice mass ratio (D/I), is uncertain (Choukroun et al., 2020), but we choose a value of 4 (Rotundi et al., 2015) and photometric measurements revealed that the comet has a low albedo of about 0.05 (Feaga et al., 2015, Ciarniello, et al. 2015, Fornasier et al., 2016). The dust properties were set for a silicate composition (Ellsworth and Schubert, 1983 and Krause et al., 2011). The solid dust density is set to 2600 kg m^{-3} (Pätzold et al. 2016, Herique et al. 2016, Fulle et al. 2017, Pätzold et al. 2019). The dust grain radius has been chosen to vary from 10^{-6} to 10^{-2} m following a power law size distribution with exponent -3.5 (e.g. Huebner et al., 2006, e.g. Marboeuf et al., 2012). These values are in agreement with results and uncertainties obtained during the Rosetta mission (Fulle et al. 2016a, Langevin et al. 2016, Merouane et al. 2017, Choukroun et al. 2020, Marschall et al. 2020a) and imply a limited amount of particles greater than 1 cm (Marschall et al. 2020a). However, a single power law may not fit properly the data over the whole dust size range and it should be noticed that while large particles are not abundant, they might represent most of the dust mass (Fulle et al. 2016). For the given parameters the bulk density of the nucleus computed with the numerical model ranged between 475 and 510 kg m^{-3}, according to volatile content, which is close to the pre-perihelion bulk density evaluated to 537.8 ± 0.6 kg m^{-3} (Pätzold et al., 2019). Similarly, the thermal inertia evolved between 60 and 90 J K^{-1} m^{-2} $s^{-1/2}$ which is in the range of the estimated thermal inertia from 10 to 150 J K^{-1} m^{-2} $s^{-1/2}$ (Groussin et al., 2019). Due to the low thermal inertia, the thermal conductivity of the nucleus layers is computed with the Hertz factor formula. The choice of thermodynamic properties and laws for ices are extensively detailed in Marboeuf et al., (2012). The model is also able to handle the different ice phases and transitions (crystalline, amorphous and clathrates). Some studies proposed the presence of different ice phases in the nucleus (Mousis et al., 2015), however, for simplicity, we only consider crystalline ices in this study.

The initial number of numerical layers was set to 500 including 50 layers with a minimum thickness of 1 mm (without dust mantle) or 5 mm (with dust mantle) immediately below the surface. These thicknesses are comparable to or thicker than the dust grains considered in our size distribution but do not properly represent the potential case in which most of the dust is contained in large particles. The thicknesses of the layers increase exponentially to the nucleus centre. The simulations were performed over several orbits with a variable time step depending on the heliocentric distance varying between 15 s to 7.5 min. All the presented results have converged both with time step and space step. For all the simulations the initial parameters presented in Table 1 were kept constant.

Parameter	Value	Reference
Semi-major axis (AU)	3.46	Maquet (2015)
Eccentricity	0.64	Maquet (2015)
Orbital period (yr)	6.44	Maquet (2015)
Aphelion position (AU)	5.68	
Aphelion date	21 May 2012	
1st Equinox position (AU)	1.67	
1st Equinox date	11 May 2015	
Perihelion position (AU)	1.24	
Perihelion date	13 August 2015	
2nd Equinox position (AU)	2.62	
2nd Equinox date	20 March 2016	
Rotation period (hr)	12.4043	Mottola et al. (2014)
Obliquity (deg)	52.25	Sierk et al. (2015), Brugger et al. (2016)
Argument of subsolar meridian at perihelion (deg)	-110.50	Brugger et al. (2016)
Comet radius (km)	2.00	
Initial porosity	75%	Taylor et al. (2017)
Pore radius (m)	10^{-4}	Huebner et al. (2006)
Dust to ice mass ratio	4.00	Rotundi et al. (2015)
Bolometric albedo	0.05	Taylor et al. (2017)
Emissivity	0.95	Spohn et al. (2015)
Initial temperature (K)	30	
Dust density (kg m^{-3})	2600	Pätzold et al. (2016, 2019)
Heat capacity of dust (J kg^{-1} K^{-1})	770	Prialnik et al. (2004)
Dust thermal conductivity (W m^{-1} K^{-1})	4.00	Ellsworth and Schubert (1983)
Range size of dust grains (m)	10^{-6} to 10^{-2}	Marboeuf et al. (2014)

Table 1: Modelling parameters for the nucleus 67P/C-G.

223 The initial bulk composition of the nucleus and the dust mantle thickness are also required as
224 input parameters. These were treated as free parameters in order to observe their influence on the
225 outgassing pattern and to fit the observations.
226
227 d. Global production rates
228
229 The thermo-physical model and input parameters provide the evolution of the absolute
230 production rate of volatiles at the surface of the spherical comet (Fig. 3). Outgassing rates obtained at
231 different latitudes (Section 2.e, Fig. 5) have also been integrated separately over the northern
232 hemisphere and over the southern hemisphere for one comet orbit. The results are scaled with a free
233 parameter referred to as the Effective Active Fraction (EAF) translating the fact that the surface of the
234 comet is not fully active. An EAF of 20% is applied to our volatiles outgassing to match the observed
235 total volatiles loss and maximum production peak (Marschall et al., 2017, 2020a, Läuter et al., 2019,
236 2020, Combi et al., 2020). This value is higher than the typical evaluated value of about 1% used by
237 other groups (Gulkis et al., 2015, Marschall, et al., 2020b), which is a consequence of the subsurface
238 sublimation processes included in the model
239

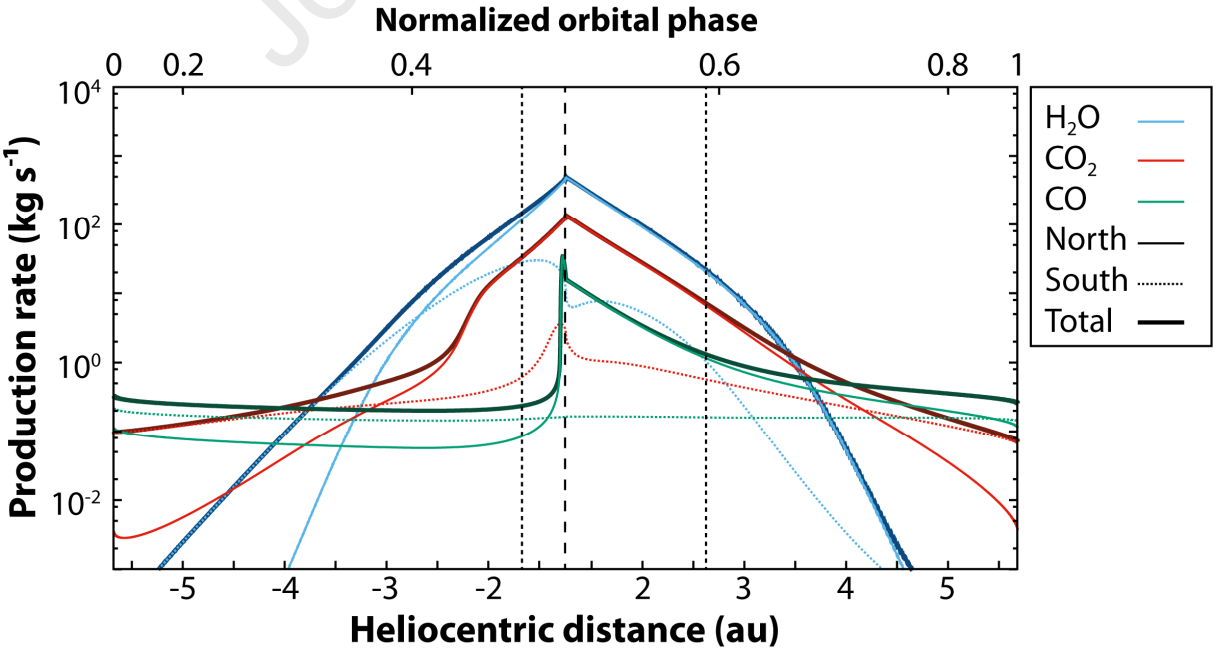

240

Fig. 3: Production rate (kg s^{-1}) of H_2O, CO_2 and CO as function of the heliocentric distance r_h (au) and normalized orbital phase. The production rates have been integrated over the spherical surface for latitudes of the northern hemisphere (December 2014 bulk composition, Table 2) and of the southern hemisphere (November 2015 bulk composition, Table 2), corresponding to solid and dotted lines, respectively. The EAF is 20%. The sum of the two hemispheres corresponds to the bold lines. The perihelion is highlighted by vertical black dashed line and equinoxes by vertical pointed black lines.

With an EAF of 20%, we obtained a total H_2O loss over the entire orbit of 7.3 x 10^9 kg which is the same order of magnitude as previous estimates from measurements (6.4 x 10^9 kg Hansen et al. (2016), 4.9 x 10^9 kg, Combi et al. (2020), 6.1 x 10^9 Marshall et al. (2020a), 4.0 x 10^9 kg, Läuter et al. (2020)). The peak of H_2O production occurs about 6 days after perihelion with a production rate of about 4.9 x 10^2 kg s^{-1} (~1.6 x10^{28} molecules s^{-1}) for the southern hemisphere and about 60 days before perihelion with a production rate of about 3.0 x 10^1 kg s^{-1} (~1.0 x 10^{27} molecules s^{-1}) for the northern hemisphere. The production rate obtained for the southern hemisphere (and the global production) is consistent with previously estimated H_2O peak production based on measurements analysis with values on the order of 5.0 x 10^2 kg s^{-1} (3.5 ± 0.5 x 10^{28} molecules s^{-1}, Hansen et al., 2016 (total H_2O production), 1.4 ± 0.5 x 10^{28} molecules s^{-1}, Marshall et al., 2017 (total production), 2.0 ± 0.1 x 10^{28} molecules s^{-1}, Läuter et al., 2019 (total production and southern hemisphere production), 2.8 x 10^{28} molecules s^{-1}, Combi et al. 2020 (total production), 2.7 x 10^{28} molecules s^{-1}, Marschall et al. 2020a, 1.8 x 10^{28} molecules s^{-1}, Läuter et al., 2020 (total production)). However, the value obtained for the northern hemisphere appears to be underestimated (by a factor of about 5) by the thermo-physical model compared to DFMS/COPS measurements analyse (H_2O peak of production rate for northern hemisphere is about 1.8 x 10^2 kg s^{-1}, Läuter et al. (2019)). In addition, our thermo-physical model does not reproduce well the time shift of peak production that is observed to be about 20 days after perihelion (Hansen et al. 2016).

With an EAF of 20%, we obtained over the entire orbit a total CO_2 loss of 2.0 x 10^9 kg and a total CO loss of 2.5 x 10^8 kg which is on the same order of magnitude as previous estimates (8.8 x 10^8 kg and 2.1 x 10^8 kg respectively, Combi et al. (2020) and 7.2 x 10^8 kg and 1.9 x 10^8 kg respectively,

Läuter et al. (2020)). The peak of CO_2 production occurs about 6 days after perihelion and gives a production rate of about 1.3 x 10^2 kg s^{-1} (~1.8 x10^{27} molecules s^{-1}) for the southern hemisphere and about 27 days before perihelion and gives a production rate of about 3.6 kg s^{-1} (~5.0 x10^{25} molecules s^{-1}) for the northern hemisphere. Finally, the peak of CO production occurs at perihelion and gives a production rate of about 3.4 x 10^1 kg s^{-1} (~7.4 x10^{26} molecules s^{-1}) for the southern hemisphere and about 3 days before perihelion and gives production rate of about 1.7 x 10^{-1} kg s^{-1} (~3.6 x10^{24} molecules s^{-1}) for the northern hemisphere. Note the difference in the time at which the maxima are reached here when compared to H_2O. As for H_2O production rates, the results obtained for the southern hemisphere match the observation for an EAF of 20% (1.6 x10^{27} molecules s^{-1} and 5.9 x10^{26} molecules s^{-1} for the maximum production of CO_2 and CO respectively, Läuter et al., 2020) while for the northern hemisphere the value are underestimated by a factor of about 5 relative to other calculations.

The total production rates are dominated by the southern hemisphere contribution within about 3.5 au in our results (Fig. 3). The slopes of the integrated volatiles production as function of the heliocentric distance (r_h) have been calculated with a power law (~ r_h^{α}) for a chosen range between -3.5 to 3.5 au corresponding to the Rosetta mission range. For H_2O, we obtained a steeper slope before perihelion than after with α values of -4.2 and -3.6 respectively. The value before perihelion is consistent with previous studies based on measurements analyses (values between -3.8 to -7.0) while our results after perihelion is lower (values between -4.3 to -7.1) (Hansen et al., 2016, Marshall et al., 2017, 2020a, Shinnaka et al., 2017, Läuter et al., 2019). Our slopes match the observations better than the significantly lower slope (about -2.8 for the model A) provided by the thermal model of Keller et al. (2015b). For CO_2, we obtained α value of -3.5 after perihelion, and for CO, we obtained α values of -3.3 after perihelion (the slope values before perihelion are not satisfactory (asymptotic standard error > 5%) fit with the power law), corresponding to slightly lower slopes obtained for the H_2O production rate after perihelion. Slopes obtained for CO_2 and CO, respectively, are lower than the slopes obtained by Läuter et al. (2019) (-4.5 and -6 for CO_2 and CO respectively).

297 The thermo-physical model provides a reasonable approximation to the volatile production
298 rates but clearly the existing model does not produce a perfect fit. For example, the different EAF
299 require to fit the production rates in the northern and southern hemisphere are likely caused by the
300 presence of a desiccated dust mantle at the surface of the nucleus for the northern plains inhibiting the
301 outgassing while ices are present up to the nucleus surface in the southern hemisphere (Section 2.e and
302 Table 2). But there are perhaps alternative structural models that could be defined that would provide
303 better fits. Nonetheless, it is encouraging that the model essentially derived from first principles can
304 approach observed values.
305
306 e. Strategy of data comparison
307
308 ROSINA collected data at different latitudes and distances from the nucleus following the
309 spacecraft orbit (Fig. 4). However, the exact location in the coma is not implemented in the numerical
310 model. Therefore we choose to study the dimensionless volatiles density ratios measured in the coma
311 by ROSINA/DFMS (CO/CO_2, CO_2/H_2O and CO/H_2O) to avoid gas density extrapolation corrections
312 caused by the spacecraft-comet distance. We also assume that the three species have the same equal
313 acceleration profiles and so the measurement of the ratios at a distance from the surface would be
314 unchanged from the surface. In addition, we ran numerical simulations for different sub-spacecraft
315 latitudes explored by Rosetta. The sub-spacecraft latitude corresponds to the angle between the
316 spacecraft projection at the nucleus surface and the equator. It is independent of the nucleus shape. We
317 consider that the projected latitude of the spacecraft on the nucleus corresponds to the latitude of gas
318 release. This approach does not capture any lateral flow that might occur as a result of the gas flow
319 dynamics (e.g. Kitamura, 1985). It should be noted that this effect can strongly influence the gas
320 densities close to the terminator and might influence ratios of species because of the different
321 molecular masses and initial velocities.
322

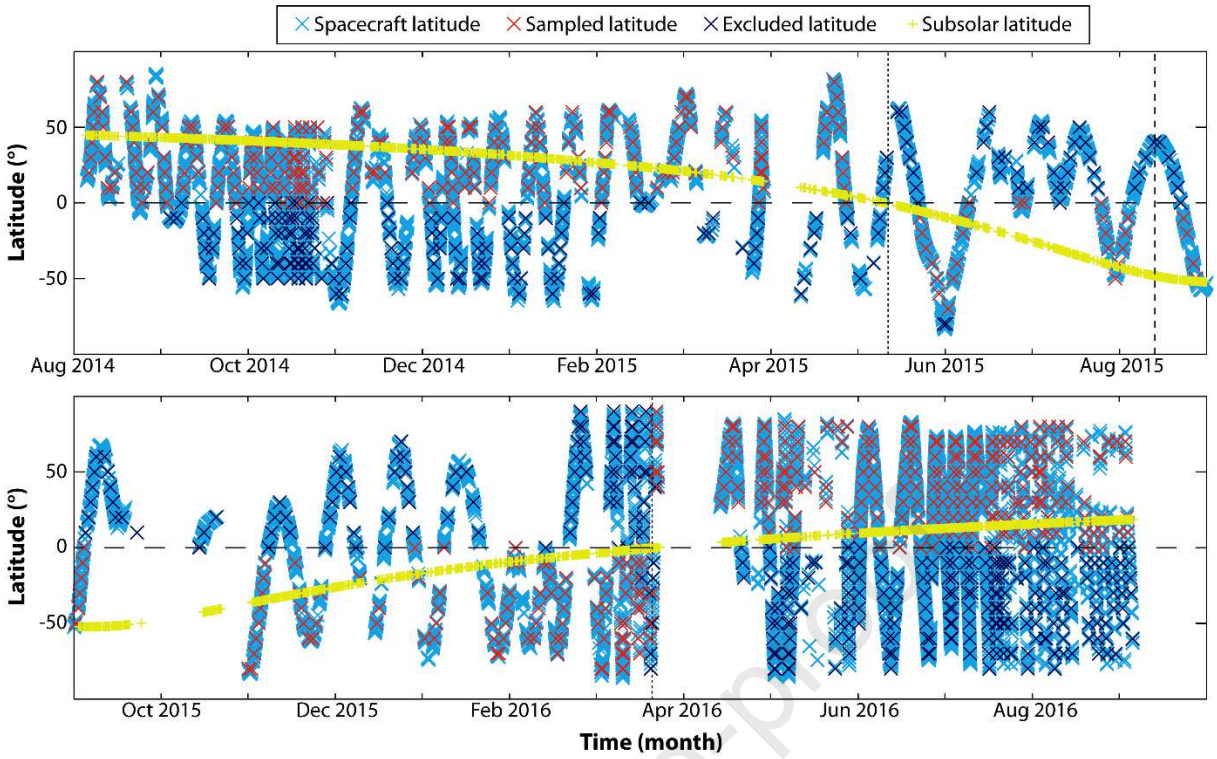

Fig. 4: Latitudes sampled by the numerical model (red crosses) compared to the Rosetta sub-spacecraft latitudes projection onto the surface (blue crosses) of the comet. Some sampled values were excluded (dark blue crosses) as numerical results are obtained for incidence angles above 90°. The subsolar latitude (yellow crosses) of the comet 67P/C-G is also indicated. The northern hemisphere is illuminated before the 1st equinox and after the 2nd equinox. Between the equinoxes and trough perihelion passage, the southern hemisphere is illuminated. The perihelion is highlighted by the vertical black dashed line and equinoxes by vertical pointed black lines.

We performed numerical simulations for latitudes between 90°S to 90°N with a 10° increment. If a ROSINA measurement was available for the given latitude (within bounds of ± 2°), we extracted the numerical result at the corresponding time (Fig. 4). Numerical results obtained for an incidence angle above 90° are excluded (Fig. 5 a and b). The calculated gas density drops drastically on the night side (Fig. 6), especially for H_2O, which might not be the case in reality because of lateral gas flow and/or non-insolation driven emission and hence comparisons at incidence angles greater than 90° are likely to be misleading. This selection excluded mostly southern latitudes results for

periods before and after the 1st and 2nd equinox, respectively, and mostly northern latitudes for period in-between the equinoxes (Fig. 5 c and d).

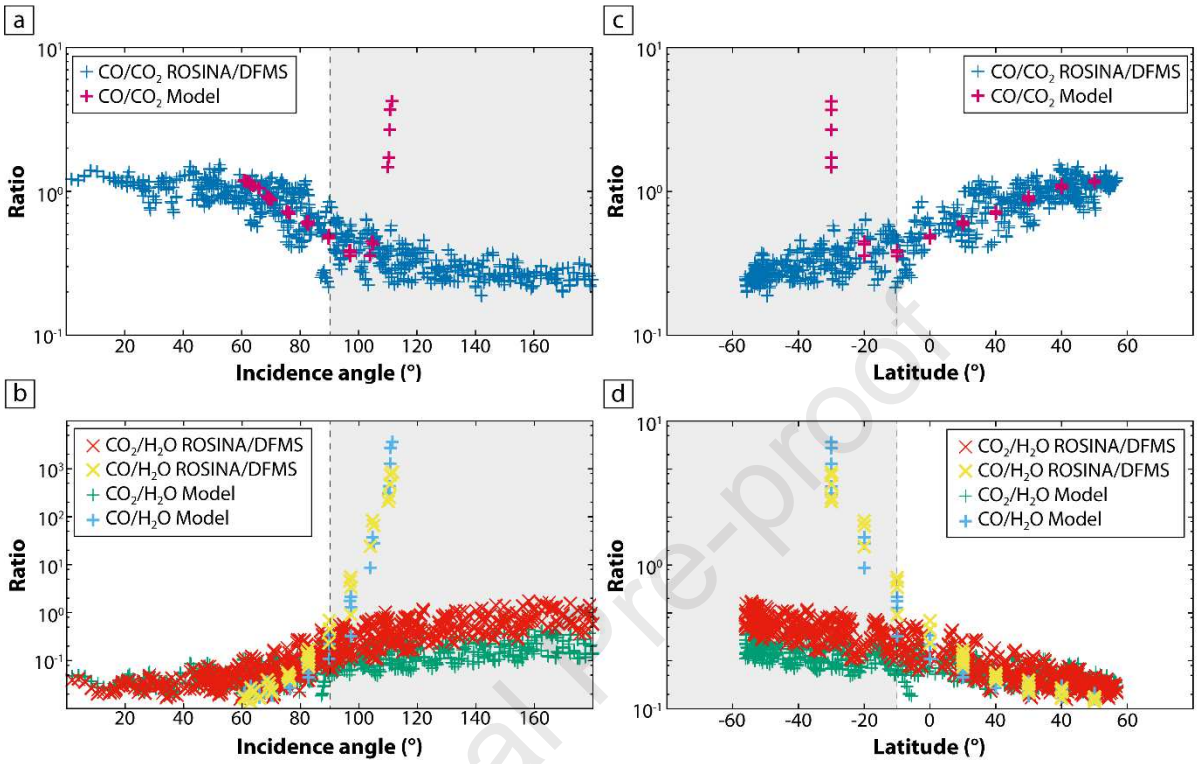

Fig. 5: Evolution of the CO/CO_2 (a) and CO_2/H_2O and CO/H_2O (b) density ratios with incidence angle of ROSINA and results from numerical modelling. Evolution of the CO/CO_2 (c), CO_2/H_2O and CO/H_2O (d) density ratios with latitude of ROSINA and results from numerical modelling. The grey areas highlight, respectively, the incidence angles (right areas on panels a and b) and latitudes (left areas on panels c and d) for which computed values diverge and are excluded for the study. Model results above 90° incidence angle (a and b left) and below latitude -50° (c and d right), respectively, are out of scale. The results are presented for December 2014.

To compare our results efficiently with the measurements we averaged the computed results of density ratios. As mentioned above, H_2O exhibits large outgassing variation over many orders of magnitude (Fig. 6) induced by its presence at or close to the surface (Section 4) and consequently is highly sensitive to illumination variations. Therefore, differences with respect to the time of the sampled data with the instrument lead to large errors in the production rate of H_2O compared to

356 experimental measurements. In addition, the outgassing of H_2O is highly dependent on the complex
357 shape of the comet and it has been shown that some areas are more active than others (Marschall et al.,
358 2017). Finally, the instrument receives contributions from adjacent latitudes/longitudes resulting from
359 the gas expansion process. This tends to smooth the signal recorded. By averaging the modelling data
360 over one comet rotation (12h40) we significantly improved the coherence of our results for the
361 comparison with ROSINA measurements (Fig. 7a). The averaging of the CO/CO_2 density ratio is less
362 affected because these species are mostly located below the surface (Section 4, Fig. 13) and are
363 therefore less sensitive to the day-night cycle. The production rate of CO_2 varies by less than 3 orders
364 of magnitude in the southern hemisphere in-between equinoxes, while it is almost constant in the
365 northern hemisphere before the 1st equinox (Fig. 6). CO outgassing is almost constant in both periods.
366

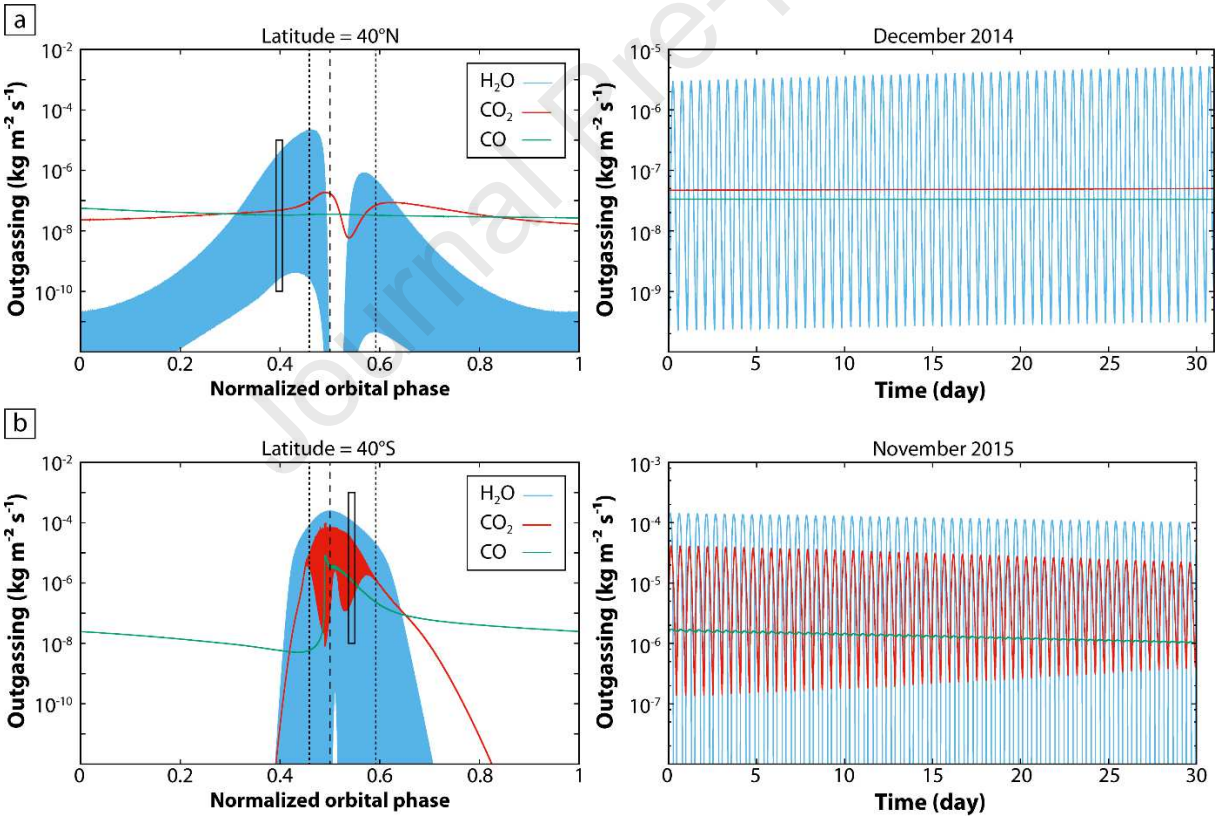

367

368 **Fig. 6:** Evolution of the outgassing rates (kg m^{-2} s^{-1}) of H_2O (blue), CO_2 (red) and CO (green)
369 computed at (a) latitudes 40°N (December 2014 bulk composition) and (b) 40°S (November 2015 bulk
370 composition) over one orbital period (~6.44 yrs). The right panels are zooms (highlighted in the left

371 panel by a black box) over one month. The perihelion is highlighted by vertical black dashed line and
372 equinoxes by vertical pointed black lines on the left panels.
373
374 To reproduce the volatiles density measured in the coma by ROSINA/DFMS, the initial bulk
375 composition of the three studied species in the nucleus were modified until we found the best
376 combination to fit the volatiles density ratios measurements in the coma with the given fixed
377 parameters (Table 1). Following, we refer to the volatiles abundance ratio, in the coma as the volatiles
378 density ratios and, in the nucleus as the volatiles bulk composition ratios. For simplicity, we split the
379 timeline according to month and found the best fit composition for each month by calculating
380 correlation criteria which are (1) the calculated density ratio over the measured density ratio averaged
381 over the given month and (2) iterating to minimize the Root Mean Square Error (RMSE, Table 2).
382 Simulation for which the calculated density ratio is different by more than 50% of the measured
383 density ratio and/or with a RMSE above 1 are considered unreliable and excluded from averaging
384 calculations. The results presented here are for different epochs but we will now focus on the results
385 for December 2014. At this time, the spacecraft was close to the nucleus (Fougere et al., 2016) and far
386 from the Sun and hence the effects of collisions in the flow and reaction chemistry in the coma were at
387 a low level. The presence of a dust mantle at the surface has also been treated as a free parameter. This
388 choice has been motivated by the fact that the presence (or not) of a substantial dust mantle at the
389 surface of 67P/C-G is a direct observation from the OSIRIS camera (Thomas et al., 2015a and 2015b)
390 and it is known that the dust mantle has an effect on the outgassing (Huebner et al., 2006, Marboeuf et
391 al., 2014). Therefore, if the addition of a dust mantle improves the fit (i.e. the calculated density ratio
392 over the measured ratio values are getting closer to 1 and/or RMSE is reduced) of the calculated
393 density ratios CO/CO_2, CO_2/H_2O and CO/H_2O with ROSINA/DFMS measurements, then we select the
394 results obtained with the dust mantle. Following testing, its thickness is kept constant at 5 mm,
395 corresponding to the best fit obtained for December 2014, and the dust grains freed from the nucleus
396 by sublimation, are assumed to escape.
397 All simulations were run first without dust mantle at the surface for several orbits until the
398 modelled nucleus reached a steady-state. In our case, this was reached after a few orbits and we choose

399 to present data obtained during the 5th orbit. After this time, the results do not evolve (Fig. 7a). This
400 corresponds to a total of time of 32.2 years which is consistent with the last major change in the orbit
401 of 67P/C-G (Maquet et al., 2015). The initiation of the dust mantle deposition at the surface of 67P/C-
402 G is unknown. It is likely that before the recent change of orbit (Maquet et al., 2015), bringing the
403 comet close to the Sun, there was no dust mantle at the surface of 67P/C-G. In addition, the dust
404 mantle experiences erosion and restoration phases (Groussin et al., 2015, Fornasier et al., 2016, Hu et
405 al., 2017). Then, in case the presence of a dust mantle is required, it has been added at the beginning of
406 the 5th orbit, disturbing the steady-state of the nucleus beyond the end of the 5th orbit.
407

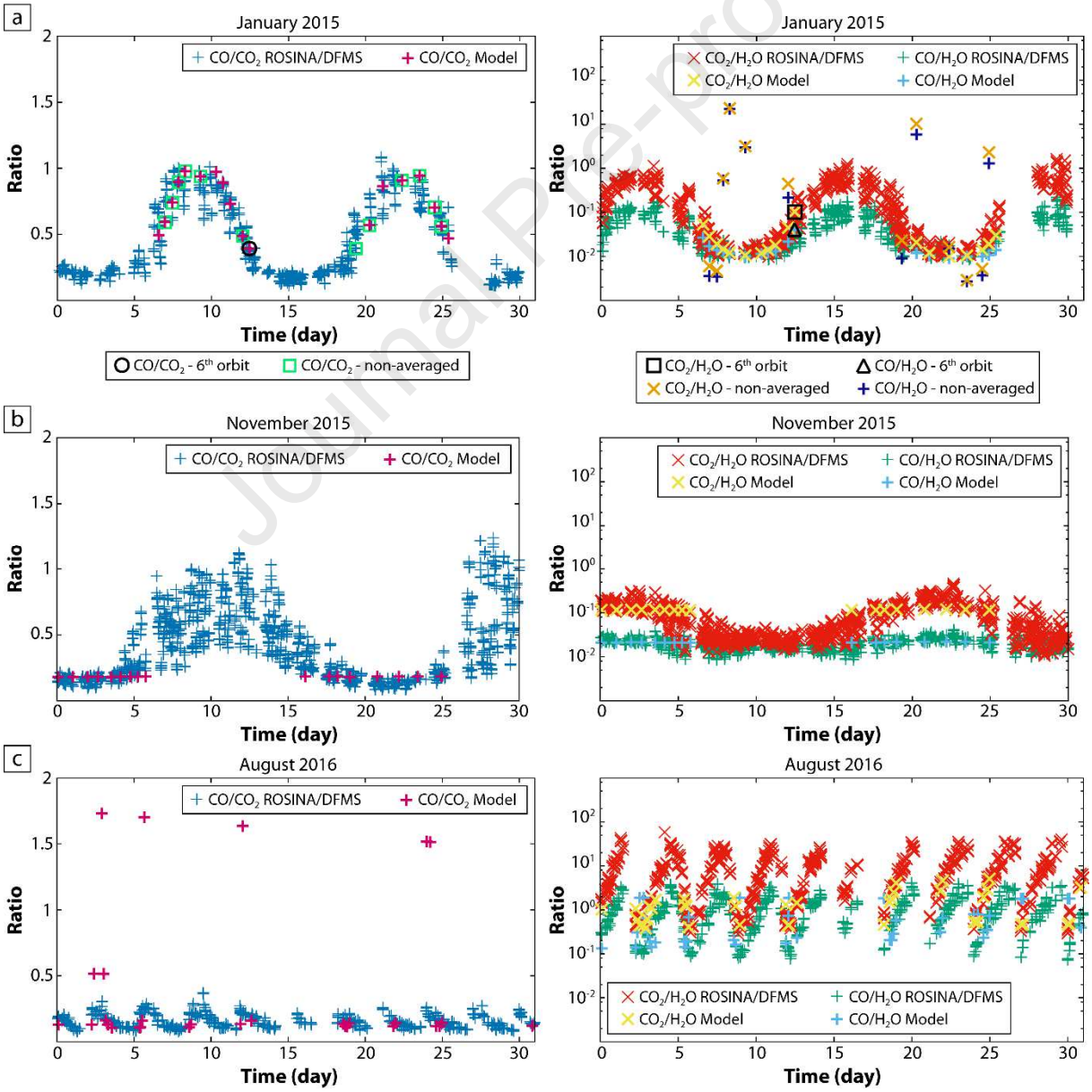

408

Fig. 7: Comparison of density ratios CO/CO_2 (left, pink crosses) and CO_2/H_2O and CO/H_2O (right, blue crosses and yellow crosses, respectively) computed by the numerical model with the data measured by ROSINA/DFMS (blue crosses, green crosses and red crosses, respectively) for (a) January 2015, (b) November 2015 and (c) August 2016. The numerical results have been averaged over one comet spin period. The bulk composition and dust mantle thickness set for each month are presented in Section 3.d (Table 2 and Fig. 12). (a) In the January 2015 plots, black circles, squares and triangles correspond respectively to CO/CO_2, CO_2/H_2O and CO/H_2O density ratios obtained at the equator and for the 6^{th} orbit (while results in pink are obtained at the 5^{th} orbit) and show that the model has converged. The light green, orange and dark blue crosses correspond to the non-averaged results of the numerical model. It does not affect the value of CO/CO_2 but might exclude some points as the incidence angle is averaged as well.

Finally, the bulk compositions of the different volatiles do not vary, at the scale of the nucleus, through the five comet orbits. Therefore the composition at the sampling time corresponds to the initial bulk composition set for each month.

3. Nucleus outgassing pattern

a. Comparison of evolution of CO/CO_2 density ratios

Our simulation results match the CO/CO_2 density ratios measured by ROSINA/DFMS satisfactory for most epochs (Figs. 7 and 8 and Table 2), especially with regards to the absolute error values of the ROSINA measured gas ratios (Section 2.a) and uncertainties in the fixed parameters (Table 1). Indeed, for the 15 months (of a total of 26) fulfilling the correlation criteria (calculated density ratio over measured density ratio is no different by more than 50% of the measured ratio and with a RMSE below 1), the average calculated density ratio over measured density ratio is 1.01 and the average RMSE is 0.23. We have established with the thermo-physical model both, (1) the correct range of magnitude of CO/CO_2 density ratios, between 1.0×10^{-2} and 3, and (2) fit the evolutionary

437 trend of CO/CO_2 density ratios, observed by ROSINA/DFMS for most parts. The CO/CO_2 density
438 ratio oscillates around 1 showing that, depending upon the time and insolation, CO outgassing can
439 surpass CO_2 and vice versa in both measurements and model. The CO/CO_2 density ratios reach values
440 of up to 3 before perihelion and below 1 for most of the post perihelion period.
441

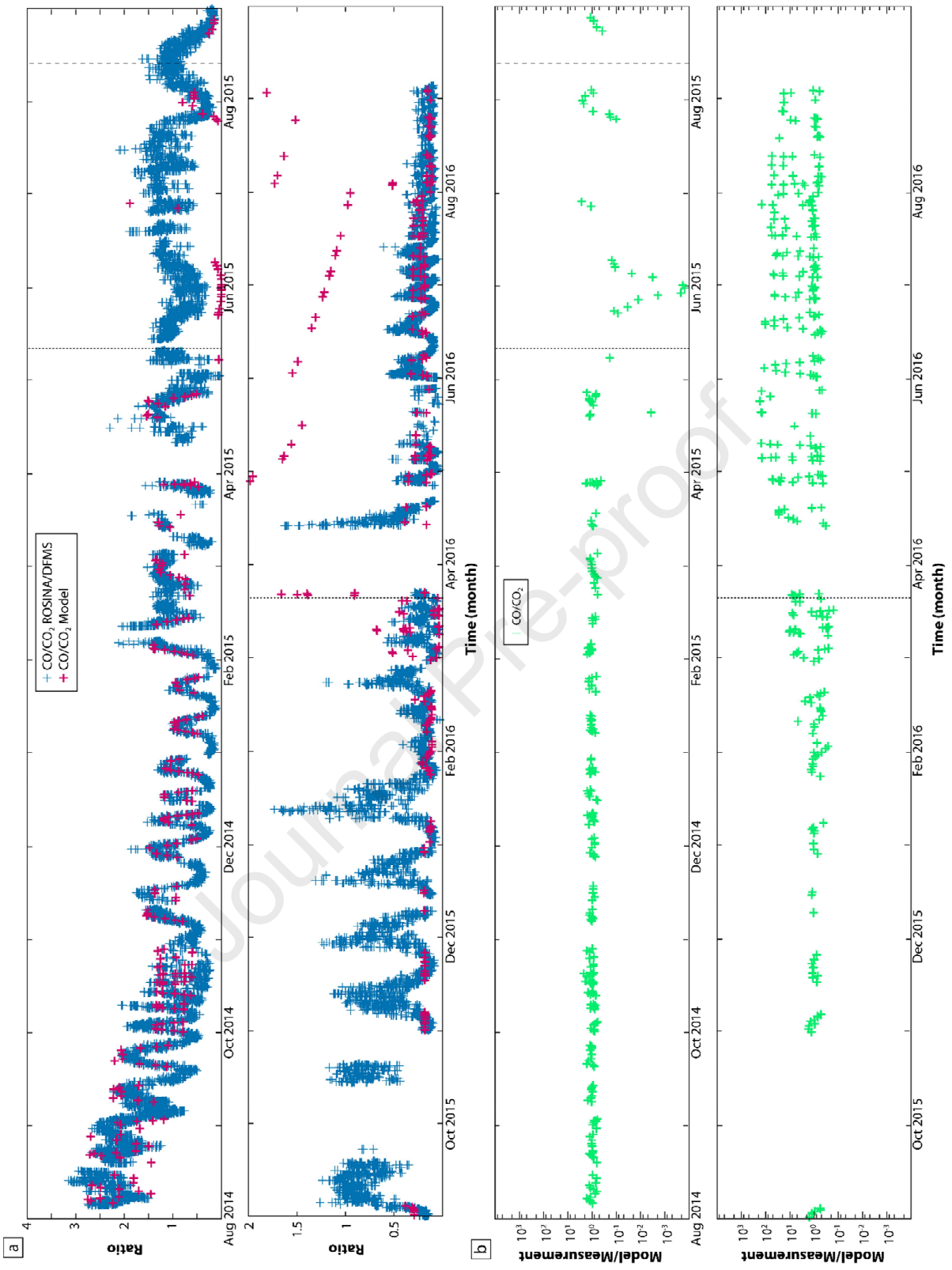

Fig. 8: (a) Comparison of the CO/CO_2 density ratio computed by the numerical model (pink crosses) with the data measured by ROSINA/DFMS (blue crosses) during the Rosetta mission. The bulk composition and dust mantle thickness set for each month are presented in Section 3.d (Table 2). (b) Ratio of the calculated to the measured CO/CO_2 density ratio (green crosses). The 1st and 2nd

447 equinoxes are highlighted by vertical black dotted lines and perihelion by the vertical black dashed
448 line.
449
450 For some months the correlation is not satisfying. This is particularly true around the
451 equinoxes (April, May and June 2015 and March, April and May 2016) with an average calculated
452 density ratio over measured density ratio of 11.3 and an average RMSE of 25.5. For these periods, we
453 have difficulty reproducing both the magnitude and the trend (Fig. 8). Despite the trend is mostly
454 reproduced for several months after the 2nd equinox (June to September 2016, although some data
455 points are out of magnitude, Fig. 7), the correlation criteria do not match with an average calculated
456 density ratio over measured density ratio of 10.53 and the average RMSE of 5.18.
457
458 b. Comparison of evolution of CO_2/H_2O and CO/H_2O density ratios
459
460 Agreements of the CO_2/H_2O and CO/H_2O density ratios with those measured by
461 ROSINA/DFMS are also satisfactory (Figs. 7 and 9 and Table 2). Indeed, for the 15 months (over 26)
462 fulfilling the correlation criteria, the average calculated density ratio over measured density ratio is
463 1.07 for CO_2/H_2O and 0.97 for CO/H_2O and the average RMSE is 0.16 for CO_2/H_2O and 0.15 for
464 CO/H_2O. We have reproduced both the magnitude and the trend for several epochs, especially
465 between November 2014 and April 2015 and between August 2015 and February 2016. Times when
466 CO_2/H_2O exceeded CO/H_2O were correctly reproduced. However, similar to the CO/CO_2 density ratio,
467 for some months the agreement between measurements and results is inferior. At the beginning of the
468 mission (August to October 2014) the trends are reproduced but not the magnitude of the ratios. As
469 with the CO/CO_2 density ratios, the fits are not satisfying for the months around the equinoxes (April,
470 May and June 2015 and March, April and May 2016), especially for CO/H_2O. The average calculated
471 density ratio over measured density ratio is 39.71 for CO_2/H_2O and > 1000 for CO/H_2O and the
472 average RMSE is 42.0 for CO_2/H_2O and > 100 for CO/H_2O. Finally, after the 2nd equinox (June to
473 September 2016), the numerical results match poorly the ROSINA measurements (Figs. 7c and 8) for
474 the CO/H_2O density ratios. The average calculated ratio over measured ratio is 21.04 and the average

475 RMSE is 6.23 for CO/H_2O. However, we notice an improvement of the fit for CO_2/H_2O density ratios
476 toward the end of the mission with an average calculated density ratio over measured density ratio of
477 1.23 and an average RMSE of 0.98. For this ratio, the trend and magnitude of the values are mostly
478 reproduced (Fig. 7c and 9 and Table 2). Because of weak reliability of the computations performed for
479 after the 2^{nd} equinox, we have focused our efforts on reducing the RMSE and matching the measured
480 value of CO_2/H_2O.
481

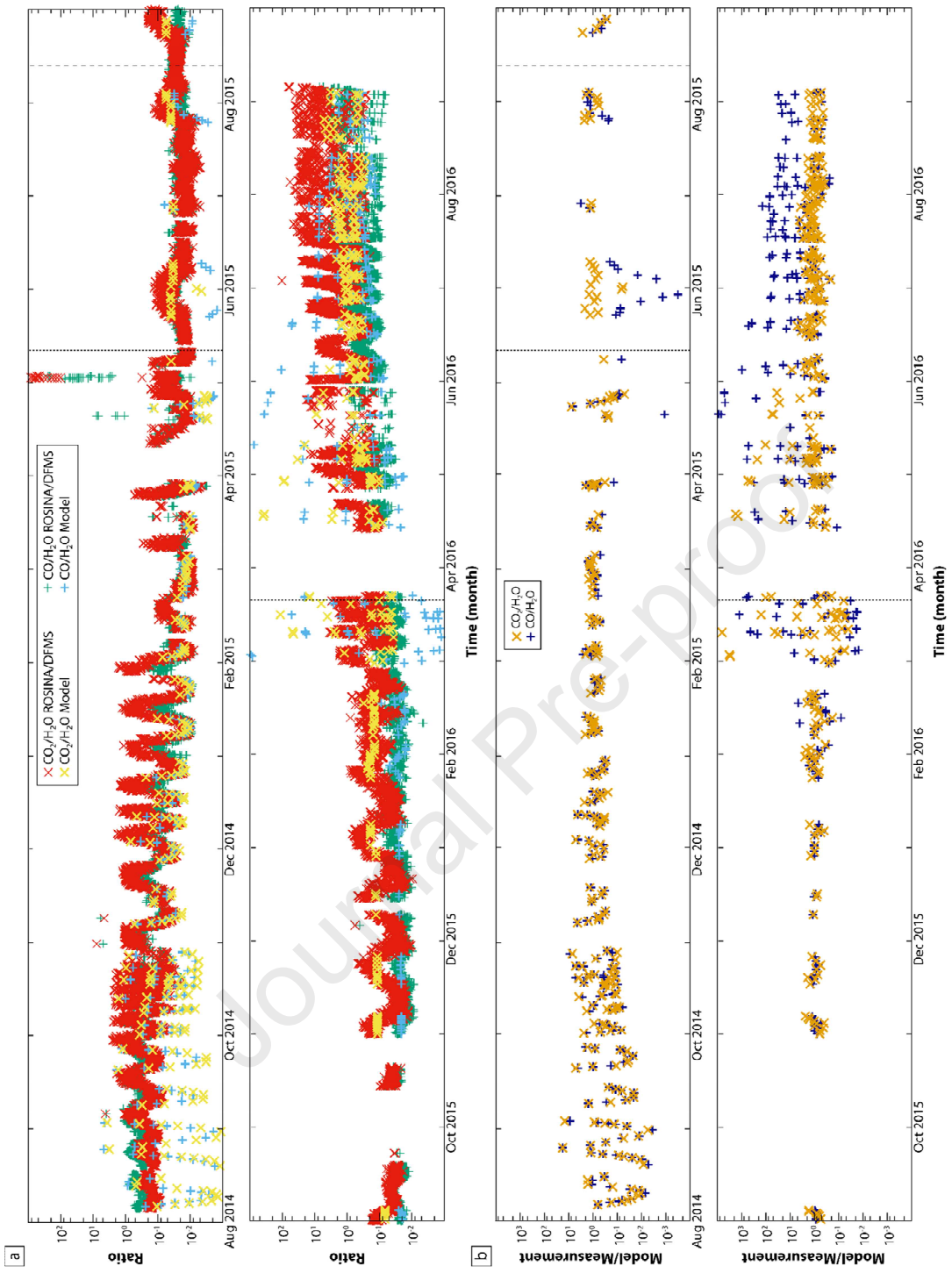

Fig. 9: (a) Comparison of CO/H_2O and CO_2/H_2O density ratios computed numerically (blue crosses and yellow crosses, respectively) with the data measured by ROSINA/DFMS (green crosses and red crosses respectively) during the Rosetta mission. The bulk composition and dust mantle thickness set for each month are presented in Section 3.d (Table 2). (b) Ratio of the calculated to the measured density ratios of CO_2/H_2O and CO/H_2O (orange and dark blue crosses respectively) during the Rosetta

mission. The 1st and 2nd equinoxes are highlighted by vertical black dotted lines and perihelion by vertical black dashed line.

c. Influence of the dust mantle

A remarkable point is that to get these fits between the model and the ROSINA/DFMS measurements, it is necessary to add a dust mantle at the surface of the nucleus (after it reached steady state without dust mantle) for simulations for periods before the 1st equinox and after the 2nd equinox while it is not necessary for simulations between the equinoxes. If no dust mantle is added for those periods, the order of magnitude remains within the observed range but the trend is no longer consistent with the measurements, particularly for the CO/CO_2 density ratios (Fig. 10).

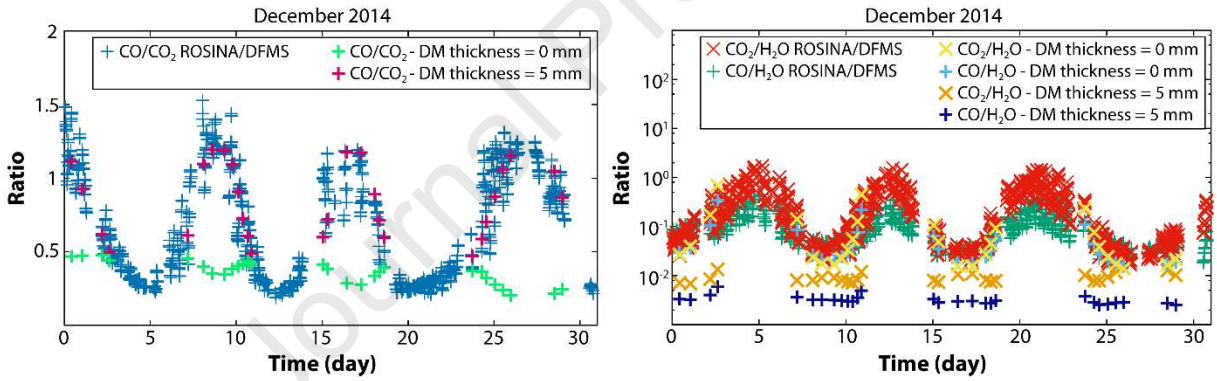

Fig. 10: Comparison of (a) CO/CO_2 and (b) CO_2/H_2O and CO/H_2O density ratios computed by the numerical model without dust mantle (DM = 0) and with dust mantle (DM = 5 mm) with the data measured by ROSINA/DFMS for December 2014.

The addition of a desiccated dust mantle increases the global thermal inertia. For instance it goes from ~62 J m^{-2} K^{-1} $s^{-1/2}$ without a dust mantle to ~71 J m^{-2} K^{-1} $s^{-1/2}$ with a dust mantle for December 2014. This favours the "storage" of heat and inhibits the immediate reaction of the nucleus surface to solar illumination changes. This increases the thermal lag and the surface temperature affecting heat transfer deeper into the nucleus (Fig. 11). The thermal wave reaches the sublimation fronts of different ices at different times as the sublimation fronts of CO_2 and CO are below the

surface in this scheme (Fig. 11 and Section 4, Fig. 13). This is contrary to H_2O which remains close to the surface in all cases. It appears that both, temperature profile and depth of sublimation fronts (Fig. 11) are critical parameters driving CO_2 and CO outgassing pattern. Changes can provoke ratio trend inversion (Figs. 10 and 11). Our results suggest that a limited change in thermal inertia, of about 10 J m^{-2} K^{-1} $s^{-1/2}$, has a strong influence on the resulting outgassing pattern.

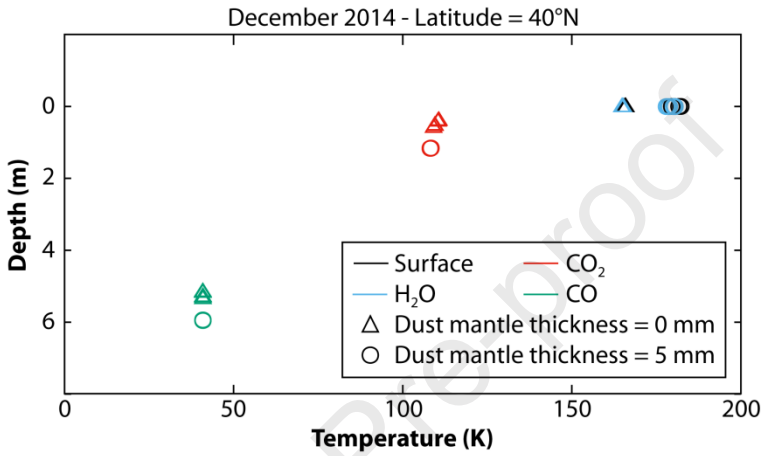

Fig. 11: Depth and temperature of the different sublimation fronts of the volatiles (H_2O: blue, CO_2: red and CO: green) and surface temperature (black) computed by the numerical model without dust mantle (DM = 0, triangles) and with dust mantle (DM = 5 mm, circles) for fit obtained for December 2014 (Fig. 10). We take as example results obtained at latitude 40°N.

d. Nucleus bulk composition and evolution

We are able to reproduce, with good agreement (see Sections 3a and 3b), the ROSINA/DFMS measurements (Figs. 8 and 9 and Table 2). Exceptions are, close to equinoxes and after the 2nd equinox. Numerical results fit the measurements at different latitudes explored by the spacecraft for a given month with a uniform volatile composition. This suggests a rather homogeneous composition of different areas of the nucleus.

Month	Initial volatiles bulk composition (wt%)	Initial volatiles bulk composition ratio	Dust Mantle	Averaged density ratio (Model/Measurements)	Root Mean Square

	H_2O	CO_2	CO	CO/CO_2	CO_2/H_2O	CO/H_2O	thickness (mm)	CO/CO_2	CO_2/H_2O	CO/H_2O	CO/CO_2	CO_2/H_2O	CO/H_2O
Aug-14	99.75	0.14	0.11	7.86E-01	1.40E-03	1.10E-03	5	1.00	1.01	0.97	5.33E-01	5.97E-01	9.15E-01
Sep-14	99.60	0.24	0.16	6.67E-01	2.41E-03	1.61E-03	5	1.03	1.17	0.90	3.61E-01	7.86E-01	9.19E-01
Oct-14	99.00	0.70	0.30	4.29E-01	7.07E-03	3.03E-03	5	1.05	0.98	0.98	2.63E-01	2.95E-01	1.96E-01
Nov-14	92.00	5.10	2.90	5.69E-01	5.54E-02	3.15E-02	5	0.99	1.00	0.98	1.79E-01	1.08E-01	9.68E-02
Dec-14	93.00	4.80	2.20	4.58E-01	5.16E-02	2.37E-02	5	1.04	1.08	1.00	1.98E-01	1.32E-01	6.38E-02
Jan-15	93.00	5.00	2.00	4.00E-01	5.38E-02	2.15E-02	5	1.05	0.97	0.99	1.37E-01	1.44E-02	7.59E-03
Feb-15	87.00	7.80	5.20	6.67E-01	8.97E-02	5.98E-02	5	0.99	1.02	1.01	2.47E-01	9.15E-03	7.41E-03
Mar-15	89.00	6.50	4.50	6.92E-01	7.30E-02	5.06E-02	5	0.97	1.04	1.03	3.33E-01	6.74E-03	1.11E-02
Apr-15	96.00	2.20	1.80	8.18E-01	2.29E-02	1.88E-02	5	0.97	1.00	0.91	1.23E+02	4.19E-02	2.07E+00
May-15	89.00	3.50	7.50	2.14E+00	3.93E-02	8.43E-02	0	0.05	0.97	0.04	6.98E-01	3.41E-02	2.87E-02
Jun-15	89.00	3.00	8.00	2.67E+00	3.37E-02	8.99E-02	0	0.47	0.93	0.56	6.76E-01	3.51E-02	2.66E-02
Jul-15	95.00	3.80	1.20	3.16E-01	4.00E-02	1.26E-02	0	1.02	1.41	0.86	4.84E-01	2.03E-02	9.83E-03
Aug-15	94.00	5.20	0.80	1.54E-01	5.53E-02	8.51E-03	0	0.99	1.17	0.96	1.93E-01	6.32E-02	1.17E-02
Sep-15	92.00	6.20	1.80	2.90E-01	6.74E-02	1.96E-02	0	1.01	1.02	0.86	1.74E-01	3.44E-02	3.87E-03
Oct-15	-	-	-	-	-	-	-	-	-	-	-	-	-
Nov-15	87.00	11.00	2.00	1.82E-01	1.26E-01	2.30E-02	0	1.04	1.08	0.97	6.31E-02	7.42E-02	6.05E-03
Dec-15	86.00	11.80	2.20	1.86E-01	1.37E-01	2.56E-02	0	1.04	1.02	1.03	4.12E-02	2.81E-02	2.10E-03
Jan-16	82.00	16.10	1.90	1.18E-01	1.96E-01	2.32E-02	0	0.99	1.04	0.96	5.55E-02	1.06E-01	1.20E-02
Feb-16	86.00	12.70	1.30	1.02E-01	1.48E-01	1.51E-02	0	0.99	1.00	1.00	1.20E-01	1.92E-01	4.84E-02
Mar-16	80.00	18.00	2.00	1.11E-01	2.25E-01	2.50E-02	0	4.98	44.31	1018.28	5.17E-01	1.34E+02	2.34E+02
Apr-16	98.50	1.30	0.20	1.54E-01	1.32E-02	2.03E-03	5	20.92	172.84	8902.40	9.05E+00	1.10E+02	1.81E+03
May-16	97.00	2.60	0.40	1.54E-01	2.68E-02	4.12E-03	5	40.41	18.21	2514.70	1.84E+01	7.72E+00	2.82E+02
Jun-16	98.00	1.70	0.30	1.76E-01	1.73E-02	3.06E-03	5	15.22	1.52	53.20	9.75E+00	6.71E-01	1.94E+01
Jul-16	98.00	1.70	0.30	1.76E-01	1.73E-02	3.06E-03	5	14.59	1.40	17.60	6.86E+00	8.68E-01	3.81E+00
Aug-16	99.00	0.96	0.04	4.17E-02	9.70E-03	4.04E-04	5	5.16	0.91	3.84	1.79E+00	8.56E-01	6.55E-01
Sep-16	99.10	0.81	0.09	1.11E-01	8.17E-03	9.08E-04	5	7.15	1.08	9.52	2.31E+00	1.51E+00	1.06E+00

Table 2: Volatiles (H_2O, CO_2 and CO) bulk composition of the nucleus used for the numerical modelling to fit the ROSINA/DFMS measurements for each month of the measurements campaign. Molar bulk compositions are expressed in percentage. The thickness (and so its presence or not) of the dust mantle is specified. The likeness between the modelling results and the measurements are evaluated by the calculated density ratio over the measured density ratios (the best match is close to 1) averaged over the respective months and with the root mean square error. Simulation for which the calculated density ratio is different by more than 50% of the measured density ratio and/or with a RMSE above 1 are considered non reliable and excluded from averaging calculations. Results are plotted in Figure 12. Black horizontal lines separate the months containing inbound or outbound equinoxes and the bold black horizontal lines mark August 2015, the month of perihelion passage.

In order to retrieve the volatiles bulk composition of 67P/C-G nucleus, we averaged the respective bulk composition used to fit the ROSINA/DFMS density measurements for each month

meeting the required correlation criteria (Section 2.d, Table 2, Fig. 12). We obtained the following volatiles bulk composition for 67P/C-G: (91.4 ± 4.5)% of H_2O, (6.7 ± 3.5)% of CO_2 and (1.9 ± 1.2)% of CO. The values obtained are consistent with previous estimation of the volatiles bulk composition of the nucleus (Table 3) from ROSINA/DFMS data pre perihelion (Rubin et al., 2019) and integration over the whole apparition using analytical approaches (Läuter et al., 2019) and Direct Simulation Monte Carlo modelling compared to ROSINA/DFMS data (Combi et al., 2020). However it presents some discrepancy with spectral measurements (Bockelée-Morvan et al., 2016, Biver et al., 2019).

	Estimation of volatiles bulk composition					
Molecule	**This study**	**Rubin et al. (2019)**	**Läuter et al. (2019)**	**Combi et al. (2020)**	**Bockelée-Morvan et al. (2016)**	**Biver et al. (2019)**
H_2O	100	100	100	100		
CO_2	7.3 ± 3.8	4.7 ± 1.4	5.9 ± 3.0	7.4	14.0 -32.0	
CO	2.1 ± 1.3	3.1 ± 0.9	2.3 ± 1.0	2.7		0.6 ± 0.1

Table 3: Comparison of the estimated bulk compositions of the three main volatiles H_2O, CO_2 and CO in comet 67P/C-G compared to previous studies based on ROSINA data performed by Rubin et al. (2019), Läuter et al. (2019) and Combi et al. (2020) and on spectral measurements, MIRO and VIRTIS-H, performed by Bockelée-Morvan et al. (2016) and Biver et al. (2019). Molecule abundance is expressed relative to H_2O abundance.

The nucleus ices compositions and the associated standard deviations of the average bulk composition obtained to fit the ROSINA/DFMS measurements show homogeneity in the sense that they are all displaying a large amount of H_2O (>82%) and CO_2 is more abundant than CO. This suggests that, to 1st order, the global composition of the nucleus is rather homogeneous. However, the model also allows us to study volatiles composition at a finer scale. Compositional variability, over the course of the comet's journey around the Sun, has been identified and is highlighted below.

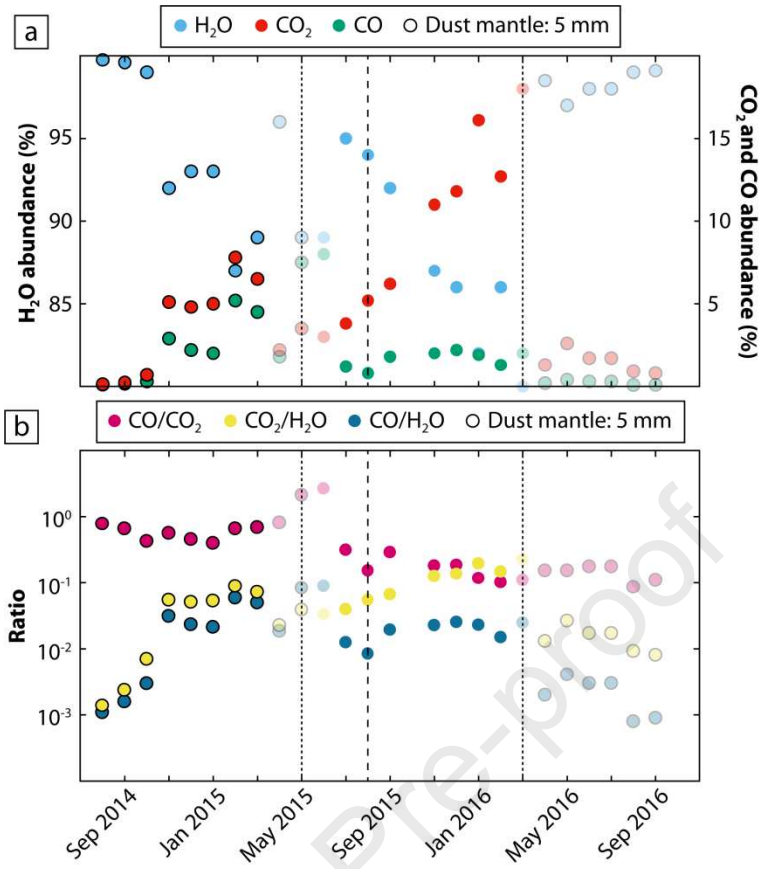

Fig. 12: (a) Evolution of the volatile bulk composition (H_2O, CO_2 and CO) used for the numerical model to fit the ROSINA/DFMS measurements for each month of the measurements campaign (Table 2). (b) Evolution of the volatiles bulk composition ratios (CO/CO_2, CO_2/H_2O and CO/H_2O) for each month of the measurements campaign (Table 2). The black circles correspond to the presence of a dust mantle (5 mm) at the surface of the nucleus in the numerical simulation. Data represented with semi-transparent colour fit poorly the measurements (Table 2) and should be considered carefully. The 1st and 2nd equinoxes are highlighted by vertical black dotted lines and perihelion by vertical black dashed line.

The volatiles bulk composition used to fit the ROSINA/DFMS measurements suggest 3 distinct patterns: (1) before the 1st equinox, (2) in between the two equinoxes and (3) after the 2nd equinox. Before the 1st equinox the averaged bulk composition is (94.0 ± 4.6)% of H_2O, (3.8 ± 2.8)% of CO_2 and (2.2 ± 1.8)% of CO which is richer in H_2O and poorer in CO_2 than in-between the two equinoxes with an average bulk composition of (88.9 ± 4.5)% of H_2O, (9.5 ± 4.2)% of CO_2 and (1.6 ± 0.5)% of CO (Table 4). The results after the 2nd equinox give an average bulk composition of (98.3 ±

583 0.7)% of H_2O, (1.5 ± 0.6)% of CO_2 and (0.2 ± 0.1)% of CO. These last values are given as an
584 indication of the trend but must be taken very carefully as the fits were not fully satisfying the
585 correlation criteria (see Section 3b and Table 2), especially the CO/H_2O density ratios. The different
586 bulk compositions for these three different periods are enhanced by the values of the CO/CO_2 bulk
587 composition ratios which are, for the given periods, broadly constant through time and with distinctive
588 values (Fig. 12b). Indeed, before the 1st equinox, the average value of CO/CO_2 is about 0.6 ± 0.1 and
589 decreases in between the two equinoxes to an average value of about 0.2 ± 0.1 (Table 4). The CO/CO_2
590 bulk composition ratios transition is clear and abrupt at the 1st equinox (Fig. 12b). Changes in the
591 outgassing evolution at the 1st equinox have already been identified by ROSINA analyses (Gasc et al.,
592 2017, Combi et al., 2020). As mentioned above, the value after the 2nd equinox must be taken very
593 carefully but it appears that the CO/CO_2 bulk composition ratio required to reproduce the
594 measurements is about 0.1 ± 0.1, which is close to the ratio obtained in-between the two equinoxes.
595
596

	H_2O (%)	**CO_2 (%)**	**CO (%)**	**CO/CO_2**
Total	91.4 ± 4.5	6.7 ± 3.5	1.9 ± 1.2	0.4 ± 0.1
Before 1st equinox	94.0 ± 4.6	3.8 ± 2.8	2.2 ± 1.8	0.6 ± 0.1
In-between equinoxes	88.9 ± 4.5	9.5 ± 4.2	1.6 ± 0.5	0.2 ± 0.1

597 **Table 4:** Volatiles bulk composition (in % ± standard deviation) of the nucleus obtained with
598 numerical modeling by comparison with ROSINA/DFMS volatiles density measurements. The values
599 correspond of the averaged of the good fits (Table 2) for the respective periods. The data after the 2nd
600 equinox are not included as they poorly fit. The averaged CO/CO_2 bulk composition ratios for the
601 respective periods are also indicated.
602
603 Finally, from one month to another, it appears that the different volatiles bulk composition
604 required to fit the measurements evolve through time (Figure 12). The H_2O percentage is high at the
605 beginning of the measurement campaign in August, September and October 2014 (> 99%) resulting in
606 CO_2/H_2O and CO/H_2O bulk composition ratios on the order of 1.10^{-3} to 1.10^{-2}. During that period the
607 CO_2/H_2O and CO/H_2O bulk composition ratios increase significantly (from 1.10^{-3} to 1.10^{-2}) due to a
608 decrease of the H_2O abundance while CO/CO_2 experiences a small decrease by a factor less than 2.

Then decrease of H_2O abundance continues until the 1st equinox to values around 88%. We notice a jump of about one order of magnitude of the CO_2/H_2O and CO/H_2O bulk composition ratios between October and September 2014 while CO/CO_2 stays rather constant. After the 1st equinox, the H_2O abundance is high again (95%) and then decreases again until the 2nd equinox (about 82%). Accordingly, bulk composition ratios CO_2/H_2O and CO/H_2O increase from July 2015 to March 2016 due to the decreases of H_2O abundance. During that period CO/CO_2 bulk composition ratios experiences a decrease of a factor ~3.

4. Nucleus internal structure

a. Chemical differentiation

The numerical model computes the equilibrium line between the gas phase and pure ice of each species within the nucleus for a given active point of the nucleus. The nucleus starts from a homogeneous composition and evolves during the revolution around the Sun to a chemically differentiated structure according to the volatility of species and thermal inertia of the nucleus (Fig. 13). The more volatile the species, the deeper is its sublimation interface. The illumination plays an important role in the species differentiation. In the studied case, H_2O is located at the surface or just below the dust mantle if present. The CO_2 sublimation interface is located within the first two meters beneath the surface. Close to perihelion, the CO_2 interface is close or even reaches the surface at southern latitudes due to fast erosion. This status remains true for several months. CO ice is the most volatile of the three studied species and therefore its sublimation interface is deeper (~ 5 metres below the surface at northern latitudes), while at southern latitudes, especially when insolation is strong close to perihelion, the CO sublimation interface can potentially reach the surface because of the rapid erosion of the surface layer. The addition of a dust mantle at the nucleus surface increases the thermal inertia leading to a deeper differentiation of CO_2 and CO species rather than without a dust mantle. Nevertheless, the low thermal inertia of the nucleus prevents a deeper chemical differentiation.

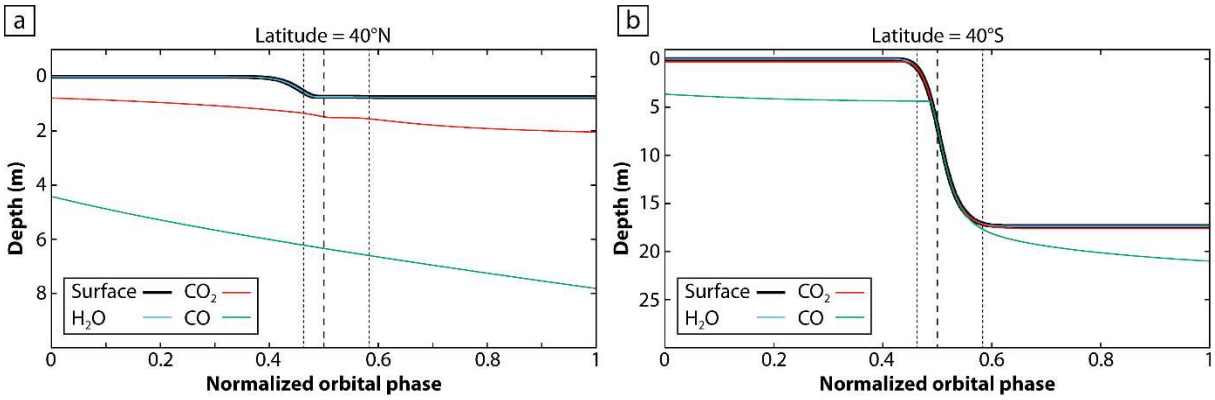

Fig. 13: Modelled internal structure of the nucleus of 67P/C-G at (a) latitudes 40°N (December 2014) and (b) 40°S (November 2015) over one orbital period (~6.44 yrs). The perihelion is highlighted by the black dashed line and equinoxes by the pointed black lines.

Spectral signatures of H_2O ice have been detected at several locations on the surface of 67P/C-G nucleus (Pommerol et al., 2015, Groussin et al., 2015, Fornasier et al., 2016). Bright H_2O ice spots are mainly observed near collapsing cliffs, dislocated boulders, and dust layered scarps. Therefore ice is present in the upper layers of the comet and can persist for several weeks but there is no wide presence of pure H_2O ice at the nucleus surface. Through perihelion, Fornasier et al. (2016) observed a change in colour towards blue suggesting an increase in the presence of water ice on the nucleus surface during this period. Spectral detection of CO_2 ice has been recorded in the southern hemisphere region, Anhur (Filacchione et al., 2016). However, authors suggested that CO_2 formed by re-condensation of CO_2 gas at the surface due to extreme changes of illumination conditions. The presence of CO_2 front deeper than H_2O is consistent with previous interpretation (Bockélée-Morvan et al., 2016, Capria et al., 2017, Biver et al., 2019). No CO spectral signature has been observed at the surface of the nucleus.

b. Surface erosion

The nucleus experiences surface erosion as the ices sublimate and the dust grains are released. We assume the comet surface displays an EAF of 20% (Section 2.d). At each orbit, for an given point active at the nucleus surface computed by the thermo-physical model, the H_2O outgassing provokes a

surface ablation of less than 1 m at 40°N latitude (with a dust mantle) and about 17 metres at 40°S latitude (without dust mantle) (Fig. 13). Our computed erosion estimation for the northern hemisphere is broadly consistent with previous calculations from thermo-physical model (taking into account the nucleus shape and only H_2O ice) with the presence of a millimetre thick desiccated layer at the top predicting less than 1 m of erosion (Keller et al., 2015b). Our estimation of the southern hemisphere erosion tends to be greater than this same model without desiccated layer at the top with only few meters of ablation, even so the maximum erosion capability of the thermo-physical model developed by Keller et al., 2015b can locally reach 20 m. However, the authors acknowledged the overestimation of H_2O ice sublimation as they considered a fully active surface leading to a H_2O production about 10 times higher compared to observation. In addition, ablation values computed by our thermo-physical model are larger than estimated based on the total mass loss of the nucleus with ablation of 0.2 m and 0.8 m respectively for northern and southern hemispheres (Pätzold Rosetta SWT 47, Keller et al., 2017). Finally, OSIRIS observations, before and after perihelion, reveal that the nucleus does not experience a global erosion of meters-scale (El-Maary et al., 2017). If so, the nucleus shape modification would have been identified at the OSIRIS pixel resolution which is up to tens of centimetres. However, locally, morphological changes and erosion have been identified in particular with dust redistribution, cliffs collapses and boulders movements (Groussin et al. 2015, Hu et al. 2017, El-Maary et al., 2017). The mass loss can reach in places up to 14 m as estimated by Fornasier et al., (2019) in the Anhur region located in the southern hemisphere.

The erosion values computed by our thermo-physical model are likely to be overestimated as the H_2O outgassing is overestimated, especially in the southern hemisphere (Fig. 3). The overestimation of the erosion might come from our numerical assumption. The considered spherical nucleus neglects the influence of shadows on the global solar input energy. However, 67P/C-G displays a complex shape (Preusker et al., 2015; Jorda el al., 2016), provoking strong shadowing effect that influence the input energy (Keller et al., 2015b). The absence of shadows leads to an enhanced volatiles production in our model. In addition, we allow the presence of ices up to the nucleus surface that will also enhance the outgassing (especially H_2O, Fig. 13). These effects are of particular

688 importance in the southern hemisphere where the energy input is stronger than in the northern
689 hemisphere (Keller et al., 2015b) and no substantial dust layer covers the surface. This effect is
690 modulated for our results in the northern hemisphere as a dust mantle at the nucleus surface is present,
691 lowering the erosion (Fig. 13). Therefore, the erosion values provided by the thermo-physical model
692 are obtained for specific assumptions and can be applied only locally for the comet 67P/C-G. Due to
693 the likely overestimation of surface erosion, the obtained values can be considered as an upper limit of
694 the erosion rate at the surface of the comet 67P/C-G.
695
696 c. Porosity
697
698 Porosity, initially set as a constant input parameter (Table 1), can evolve as the comet orbits
699 around the Sun and experiences higher temperatures and ice phase changes. Within the model,
700 condensation in the pore space of the nucleus can lead to changes in porosity. For both presented cases
701 in Figure 14, simulations at northern and southern latitudes (and with or without dust mantle
702 respectively at the surface of the nucleus), porosity profiles varied mainly within the 1st meter below
703 the surface. Just below the surface, the porosity decreases by between 5% and 11% compared to the
704 initial porosity leading to a “hard” thin (about few centimetres) layer. Additional peaks, weaker and
705 broader, occur below in both cases. For the southern hemisphere a second peak occurs about 10 cm
706 below the surface and for the northern hemisphere one occurs about 1 m and a second one deeper at
707 about 5 m. Below the deepest peak the porosity retains its initial value. Unsurprisingly, the porosity
708 minima are correlated with the sublimation front of each species as they are located at similar depths
709 (Fig. 13). Therefore each species interface leads to a porosity anomaly. Only two peaks are observed
710 for the southern latitude case because the H_2O and CO_2 interfaces are close to each other at perihelion
711 for which porosity profiles have been computed.
712

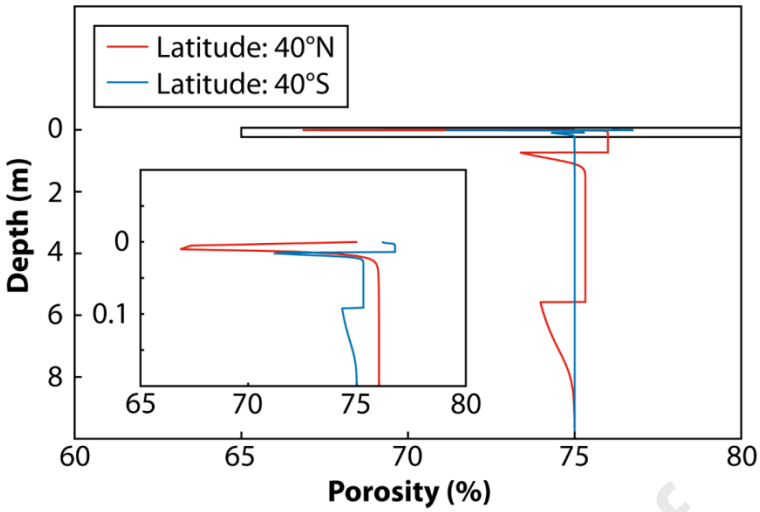

Fig. 14: Porosity profiles of the modelled nucleus trough depth at latitudes 40°N (December 2014, red line) and (b) 40°S (November 2015, blue line). The results presented represent the situation at perihelion. Initial porosity of the nucleus was set at 75% (Table 1). The surface corresponds to the sublimation front of H_2O.

The variation of porosity is consistent with numerical models (Kossacki et al., 2015, Attree et al., 2017), laboratory experiments (Kochan et al., 1989, Poch et al., 2016), geomorphologic observations of 67P/C-G (Auger et al., 2017) and in-situ measurements performed by Rosetta's lander Philae in the Abydos region (Spohn et al., 2015, Knapmeyer et al., 2018). The results either predict or have measured a hardened layer within the first centimetres and up to 1 meter below the surface of the nucleus. Re-condensation of the gas phase present in the pore of the nucleus and sintering effects create bonds between the ice grains that form a "hard" layer in the sub-surface. At Philae's landing site, the MUPUS instrument was not able to drill into the nucleus material. It was suggested that the instrument encountered a hard layer within the first centimetres below the surface. The porosity of this "hard" layer on 67P/C-G was estimated to be between 30% and 65% depending upon the nature of the refractory material (Spohn et al., 2015). However, these values are lower than the ones computed with our numerical model (Fig. 14).

5. Interpretation and discussion

734 a. Insolation driven outgassing

735

736 The thermo-physical model is able to reproduce several volatiles density measurements of
737 ROSINA/DFMS in the coma with a given volatiles bulk composition of the nucleus for different
738 latitudes explored during a given month. In addition, the bulk composition of the nucleus presents
739 some homogeneity (Section 3.d and Figs. 12 and 15 and Table 2). Both observations suggest that, to
740 1st order, the chemical outgassing pattern is mainly insolation driven rather than due to strong
741 chemical heterogeneities. This is consistent with previous studies (De Sanctis et al., 2010, Fougere et
742 al., 2016, Schroeder et al., 2019). The thermo-physical model is 1D and does not take into account the
743 complex shape of the nucleus but the model would suggest that the heterogeneities detected in the
744 coma composition (Hässig et al., 2015) are mainly driven by the tilt of the rotation axis and the
745 comet's eccentric orbit (Table 1).

746

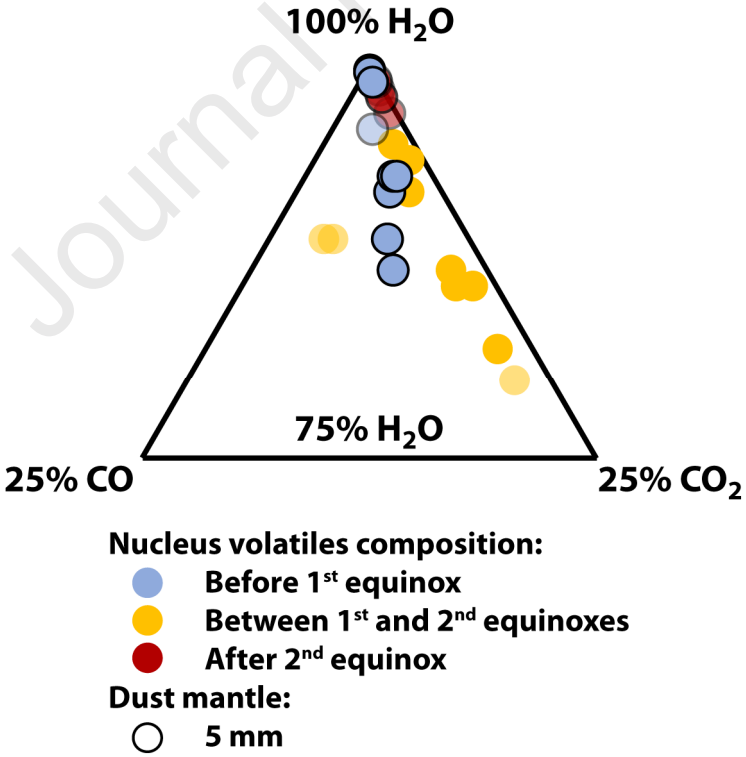

747

748 **Fig. 15:** Ternary diagram of volatiles species (H_2O, CO_2 and CO) bulk composition required to fit
749 ROSINA/DFMS volatiles density measurements. Distinction between data before the 1st equinox (blue
750 circles), in between the two equinoxes (yellow circles) and after the 2nd equinox (red circles) are

751 highlighted. Data represented with light colour fit poorly the measurements (Table 2) and should be
752 considered carefully. The presence of a dust mantle (black circle) is also specified.
753
754 b. Dichotomy
755
756 Although our results show that the nucleus displays to 1st order homogeneity in the volatile
757 bulk composition, it also reveals a dichotomy in composition between the period before the 1st equinox
758 and the period in between the two equinoxes (Figs. 12 and 15 and Table 2) that influence the
759 ROSINA/DFMS volatiles density measurements. The dichotomy is mainly highlighted by the
760 averaged value of the CO/CO_2 bulk composition ratios before the 1st equinox (0.6 ± 0.1) and in-
761 between the two equinoxes (0.2 ± 0.1). This discrepancy could either reflect a change of physical
762 properties at the surface during the 1st equinox or a difference in bulk composition between the
763 northern and southern hemispheres. The later hypothesis is favoured as the northern latitudes are rather
764 exposed to illumination before the 1st equinox and after the 2nd equinox while the southern latitudes are
765 rather exposed in-between equinoxes (Keller et al. 2015b, Fig. 4). The volatiles bulk composition
766 computed before the 1st equinox and in-between equinoxes reflect the contribution to the outgassing
767 pattern of the northern and southern hemisphere respectively (Fig. 16). Therefore, the southern
768 hemisphere appears to be less depleted in highly volatile species as chemical differentiation is less
769 deep below the surface in the South (Fig. 13). This dichotomy has been noted as well by Hoang et al.
770 (2019). As perihelion occurs between the two equinoxes, the North experienced a long and "cold"
771 summer while the South experienced a short and "warm" summer that could result in altered volatile
772 bulk compositions. However, we are not able to reproduce this behaviour with the numerical model as
773 the bulk composition of volatiles in the nucleus at the end of the simulation (5th orbit) is similar to the
774 initial composition set. Additional investigations should be performed to study the long term evolution
775 of the volatiles bulk composition of the northern and southern latitudes.
776

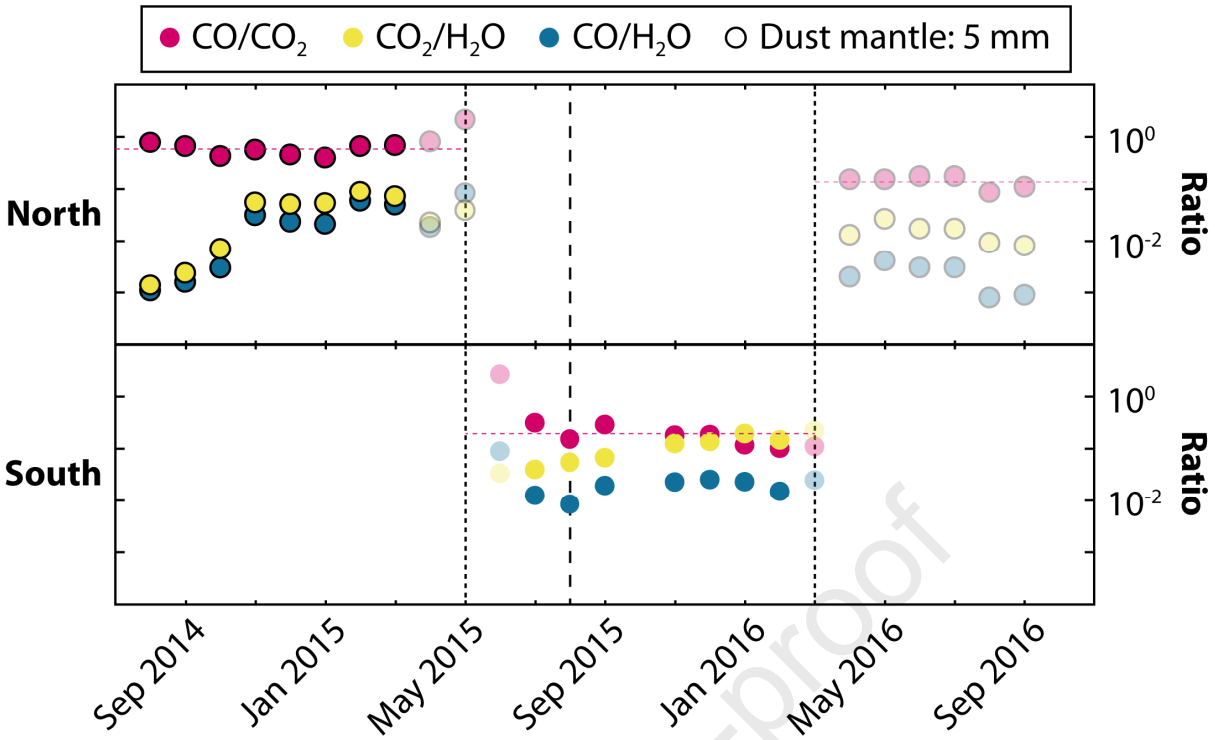

Fig. 16: Evolution of the volatiles bulk composition ratios (CO/CO_2, CO_2/H_2O and CO/H_2O) of the nucleus for each month of the measurements campaign (Table 2) and as function of nucleus hemisphere. Discrimination of the data between North and South has been obtained from the sampling strategy described in Section 2.d. This excludes southern latitudes before 1st equinox and after 2nd equinox and northern latitude in between equinoxes as results are obtained for incidence angle above 90° (Fig. 4). The horizontal pink dashed lines indicate the average values of the CO/CO_2 bulk composition ratio for a given period. The black circles correspond to the presence of a dust mantle (5 mm) at the surface of the nucleus in the numerical simulation. Data represented with light colour fit poorly the measurements (Table 2) and should be considered carefully. The 1st and 2nd equinoxes are highlighted by vertical black dotted lines and perihelion by vertical black dashed line.

To fit the data before the 1st equinox, it is necessary to modify the time lag of the thermal wave propagation through the nucleus interior to reproduce the volatiles outgassing pattern acquired by ROSINA/DFMS. In our model, this is done by the addition of a desiccated dust layer at the surface at the beginning of the selected orbit. Although we acknowledge that other physical parameters could potentially have a similar effect on the temperature profile and need to be explored (Section 5.f), the addition of the dust mantle is consistent with surface observations. During the pre-1st equinox phase,

illuminated areas of the comet are mainly located in the northern hemisphere where the presence of a dust mantle at the surface has been observed and is dominated by back falling particles (Thomas et al., 2015a and 2015b; Keller et al., 2015b) while southern areas, more exposed to the Sun between the two equinoxes, exhibit more dust-free surfaces. The dust mantle has been observed to be eroded by outgassing and restored by dust particle transport and back falling (Groussin et al., 2015, Fornasier et al., 2016, Hu et al., 2017) at the surface of the nucleus through perihelion passage. Thus, these changes will provoke disturbance of the heat wave propagation trough the interior from one orbit to another, influencing the outgassing pattern. The presence of the dust mantle also affects the depletion in volatiles enhancing the compositional dichotomy and contributes to the morphology differences between the northern and southern hemispheres (Keller et al., 2015b, 2017, El-Maarry et al., 2016).

c. Discrepancy at equinoxes and after the 2nd equinox

After the 2nd equinox, the thermo-physical model fits sometimes CO_2/H_2O density ratios but poorly CO/CO_2 and CO/H_2O density ratios (Table 2, Figs. 8 and 9). In this period, only the northern latitudes values are sampled by the thermo-physical model because of incidence angle constraint (Fig. 4). As for the period before the 1st equinox, a dust mantle is required to reproduce the trend of CO_2/H_2O density ratios. Even so, the values have to be taken carefully due to the low correlation values (Table 2). The averaged CO/CO_2 bulk composition ratio value (0.1 ± 0.1) required to get close to the measurements is closer to the ones in between the two equinoxes (0.2 ± 0.1) for which southern regions were illuminated. So it appears that the outgassing behavior after the 2nd equinox is a mixture between the southern and northern hemisphere contribution. We interpret this as the fact that the outgassing signature of the southern plains is dominating the ROSINA/DFMS measurements from the 2nd equinox until the end of the Rosetta mission and non-radial outgassing become important (Läuter et al., 2019). It affects in particular CO. Because of its volatility, these species is mostly present several meters below the surface and thus less affected by direct surface illumination variation but rather driven by thermal inertia (Fig. 13). Outgassing of CO_2 has been observed in areas that were non-illuminated (Bockélée-Morvan et al., 2016). Although the thermal inertia of the comet is low, it has an

influence on the outgassing pattern and should not be neglected when interpreting the outgassing behavior of 67P/C-G. We can also notice that toward the end of the mission the fits improve with values of the calculated density ratio over the measured density ratio getting closer to 1 and the decrease of the RMSE (Figs. 8 and 7, Table 2). That might translate the weakened of the southern regions in the outgassing contribution.

Similarly, to explain the poor fit around the 1st equinox (Table 2), we assume that this "contamination" affects measurements while the illumination moves from the northern hemisphere toward the southern hemisphere (Fig. 4). The effect might be less profound because the northern hemisphere has not experienced the intense illumination associated with perihelion.

d. Volatile evolution

The observed evolution of the volatiles through time can be significant as for instance the jump observed of the CO_2/H_2O and CO/H_2O bulk composition ratios in between October 2014 and November 2014 (Section 3d, Fig. 12). It might be due to several hypotheses that need to be investigated in the future. A first hypothesis could be that while an area starts to be illuminated, not only the volatiles species present in the nucleus start to sublimate but also the gases that have re-condensed at the surface/sub-surface in case of a drastic temperature change. Numerical calculations have estimated that the back-flux can represent up to few percent of the total outgassing (Rubin et al. 2014, Liao et al. 2018). The condensation of gases at the surface can lead to the deposition of micrometres thickness frost layer (Liao et al. 2018) that is consistent with Rosetta observation. For instance, spectral measurements suggest of a H_2O frost cycle (De Sanctis et al., 2015, Filacchionne et al., 2020) and the presence of potential CO_2 frost (Filacchionne et al., 2016). Frost may potentially condensed and be preserved on both northern and southern hemispheres followed by sublimation as it comes closer to the Sun. We speculate that this could explain the decrease of H_2O abundance, once for periods before the 1st equinox and once for periods in between the two equinoxes due to the sublimation of frost. This effect would be less important for CO_2 or CO as the bulk composition ratios CO/CO_2 are broadly constant for the respective periods. Presence of H_2O ice has also been detected in

851 the dust mantle (Groussin et al., 2015, Fornasier et al., 2016) and could influence the outgassing of the
852 northern plains as well. A second hypothesis could be related to the evolution of physical parameters
853 such as local dust mantle thickness. The dust mantle prevents H_2O from sublimating but on 67P/C-G it
854 has been observed to be eroded/shaded due to gas activity revealing H_2O water ice signatures
855 (Groussin et al., 2015, Fornasier et al., 2016, Hu et al., 2017). Therefore we speculate that the decrease
856 of H_2O abundance may be an artefact due to the actual thinning of the dust mantle itself by affecting
857 the H_2O outgassing. However, it should not/less affect the southern plains.
858
859 e. Internal heterogeneities
860
861 Our numerical simulations start with a homogeneous nucleus that then evolves as it orbits the
862 Sun. Our results revealed that the outgassing pattern of the coma is mainly driven by insolation with
863 no strong heterogeneities in the nucleus composition. It suggests that the initial material forming the
864 67P/C-G nucleus might have potentially been chemically homogeneous. However, our results cannot
865 rule out the possibility that there was at least some minor degree of heterogeneity. The North-South
866 dichotomy may have developed before the nucleus reached its current rotation axis inclination. We are
867 unable to reproduce this evolution from a single homogenous initial bulk composition of the nucleus
868 in the current orbit. The potential initial homogeneity of the nucleus might be strengthened by the fact
869 the numerical model do not detect differences (with non-averaged results, Fig. 7a) of density ratio
870 CO/CO_2 between the two lobes of the comet for different sub-spacecraft position during a given
871 month. The bi-lobate shape of 67P/C-G nucleus is may be the result of a low velocity impact between
872 two objects (Massironi et al., 2015). The North and South hemispheres include both these lobes but we
873 only detect a North-South dichotomy. Thus the two lobes might have similar initial bulk composition
874 (as suggested by Schroeder et al. (2019) looking at the D/H ratio in the water of the two lobes) and
875 have then evolved accordingly.
876 Vertical chemical heterogeneities of the nucleus form as the sublimation interface of ices
877 receded when the nucleus comes to the inner solar system and is illuminated by the Sun. As shown in
878 Figure 13, the first meters below the surface in the North and in the South are experiencing chemical

879 differentiation leading to a “layered” structure of the nucleus according to the volatility of the ices
880 (Prialnik et al., 2004, De Sanctis et al., 2010, Marboeuf et al., 2014, Fougere et al., 2016, Capria et al.
881 2017). In this study, we only investigate three species, but more volatile species will lead to a deeper
882 differentiation. Below the deeper sublimation interface we expect that the cometary material is pristine
883 unless other physical effects have been at work.

884 Lateral chemical heterogeneities at the same radius are created by different surface
885 illumination. The complex shape of the nucleus in addition to the tilt of the rotation axis lead to
886 different illumination that drives variations of the ice sublimation rate through time for adjacent
887 regions leading to horizontal chemical heterogeneities (Guilbert-Lepoutre et al., 2016). In addition, the
888 lateral heterogeneities will also be controlled by the repartition of active areas taking into account in
889 the EAF parameter (Marschall et al. 2020b). Interaction of both parameters might lead to the formation
890 of different sub-surface structures.

891 As for chemical heterogeneities, physical heterogeneities can form the same way. For instance
892 sublimation/condensation of volatiles lead to grain and porosity evolution (Fig. 14) which in turn will
893 affect the thermal properties of layers and the outgassing (Kossacki and Czwechowski 2019). In
894 addition, release of dust particles by sublimation and transport and deposition of dust particles from
895 the South to the North (Keller et al., 2015b) build a dust mantle with various thicknesses that will
896 affect the properties of the nucleus.

897 The presence of local chemical and physical heterogeneities could explain the morphological
898 diversity observed at the surface of the comet (Thomas et al., 2015a).

899

900 f. Physical properties sensitivity

901

902 Besides the potential source of error stated in Section 2c, uncertainty in the physical properties
903 of the nucleus (Table 1) can potentially affect the outgassing pattern and lead to discrepancies between
904 the measurements and the numerical results. An example is the dust properties. In the thermo-physical
905 model we estimated the dust mantle to be millimetres thick, whereas the dust mantle thickness is
906 variable and may reach several metres locally (Thomas et al., 2015b). This estimation of dust mantle

907 thickness might therefore reflect an average dust thickness at the surface of the nucleus where activity
908 is most profound. Another influence could be that the intrinsic parameters set for the dust are not
909 optimized. Indeed, we used parameters for silicate dust but the dust composition is complex and
910 difficult to constrain with a significant contribution of organics components (Quirico et al., 2016,
911 Bardyn et al. 2017). It further influences the physical properties of the dust affecting the density,
912 thermal conductivity, and heat capacity of the surface layer. In our model the dust particles are
913 modelled as spheres but observed and collected particles (by COSIMA and GIADA) present various
914 morphologies with sometimes a high porosity inferring low particle density < 1500 kg m^{-3} (Fulle et al.,
915 2017, Merouane et al. 2017). Even though the model cannot take into account complex dust shapes, a
916 size-dependant density law could be used to evaluate the influence of the particle density on the
917 outgassing (Merouane et al. 2017). In the same way, the dust-to-ice mass ratio value is quite debated
918 (Choukroun et al., 2020) and can potentially affect the outgassing pattern.

919 Further exploration of the range of the different free parameters would help to get towards a
920 more realistic model and estimation of the characteristics of the 67P/C-G nucleus. Variation of
921 parameters value might have a similar effect to the addition of a dust mantle highlighted in this study
922 (Section 3.c) or improve the fits. This would be interesting in particular to improve the fit of CO_2/H_2O
923 and CO/H_2O density ratios for the simulations performed at the beginning of the mission (August to
924 October 2014) as, even if the results match our correlation criteria (Section 2.d), the RMSE values are
925 significantly higher and closer to our threshold value of 1 (0.58 for CO_2/H_2O and 0.68 CO/H_2O
926 averaged for the 3 first months) than the ones obtained for other months (0.07 for CO_2/H_2O and 0.02
927 CO/H_2O averaged for the remaining month that have match our correlation criteria). For instance,
928 modifying parameters values could help to minimize the variation in amplitude (Fig. 9) and might
929 influence the volatiles abundances. Similarly, the estimated erosion performed by the thermo-physical
930 model appears to be larger than the observation (Section 4.a). In the South the erosion is so strong that
931 it could potentially expose both CO_2 and CO ice for several months (Fig. 13) but those ice exposures
932 were not detected during Rosetta mission. Finally, the thermo-physical model tends to underestimate
933 the porosity range in the 1st meter of the nucleus. That can be explained by several parameters such as
934 (1) incorrect characteristics of the refractory material (dust mantle thickness, dust-to-ice mass ratio,

dust conductivity and heat capacity…) influencing the thermal inertia, (2) the grains and pore sizes and/or (3) the non-implementation of the sintering process between the grains in the numerical model that can lead to an underestimation of the layer hardening.

g. Benefit of the thermo-physical model compared to previous studies

Our results have shown a good agreement with previous studies that have either directly integrated the bulk loss of volatiles measured by ROSINA/DFMS measurements (Rubin et al., 2019) or performed a model inversion of the ROSINA/DFMS measurements (Combi et al., 2020, Läuter et al., 2019). Comparison to spectral measurements (Bockelée-Morvan et al., 2016, Biver et al., 2019) show larger discrepancies, especially with CO_2/H_2O bulk composition which might be due to lower H_2O abundance derived from VIRTIS-H instrument compared to ROSINA near perihelion, while CO_2 match fairly. It is to be noted that we have used a thermo-physical model in the attempt to directly reproduce the ROSINA/DFMS volatiles density measurements with the sublimation of the nucleus orbiting around the Sun with a given bulk composition. We acknowledge that our model reproduces only partially the observed production rates (Section 2.d, Fig. 4). Peaks of volatiles production rate in good agreements with observations in the northern hemisphere or overestimated in the southern hemisphere. However, the production rate slopes provided by the thermo-physical model are closer to observations than similar thermo-physical model (model A, Keller et al. 2015b) based on first principles approach.

In addition to chemical composition of the nucleus, this direct approach provides us with some additional insight on the physical parameters that can influence the outgassing pattern and then explain the different trends we observe. For instance, we have highlighted in this study both the compositional dichotomy between the northern and southern hemispheres and the importance of the thermal inertia in the outgassing pattern. This model can be adapted to study other comets outgassing in the future.

6. Conclusion

We used a thermo-physical model with a spherical cometary nucleus to reproduce the volatiles density ratios detected in the coma of 67P/C-G by ROSINA/DFMS. For an EAF of 20%, the thermo-physical model provides a reasonable approximation of the global volatiles production rates observed. The production slopes are close (although mostly lower) than the slope obtained for observations and the volatiles peak production rates are consistent for the southern hemisphere but are underestimated in the northern hemisphere by a factor of about 5. In addition, the time of the total H_2O peak production is shifted of several days closer to perihelion compared to observations.

With the model, we reproduced the trend and order of magnitude of three density ratios CO/CO_2, CO_2/H_2O and CO/H_2O for several months of the Rosetta mission. The volatiles bulk composition used to reproduce the measurements at different latitudes for each month of the Rosetta mission present some homogeneity with $H_2O > 82\%$ and CO_2 abundance larger than CO. Nonetheless, this results in a heterogeneous coma, as has been observed for 67P/C-G by the various Rosetta payload instruments. This indicates that the outgassing is mainly insolation-driven. Specifically the strong heterogeneities observed in the 67P/C-G coma most probably result from the tilt of the spin axis and the eccentricity of the comet rather than the complex shape of the nucleus. This study provides an absolute estimation of the global volatiles bulk composition of 67P/C-G's nucleus, namely $(91.4 \pm 4.5)\%$ H_2O, $(6.7 \pm 3.5)\%$ CO_2, and $(1.9 \pm 1.2)\%$ CO.

Even though the nucleus bulk composition exhibits a global homogeneity, our study reveals a distinct composition before the 1st equinox and the period in between the two equinoxes. Indeed, before the 1st equinox the average bulk composition ratio CO/CO_2 required to reproduce the measurements is larger (0.6 ± 0.1) than the one used to reproduce measurements in between equinoxes (0.2 ± 0.1). In addition, before the 1st equinox the addition of a dust mantle (5 mm), and thus a change in thermal inertia, is required at the nucleus surface to fit the experimental data while it is not the case in-between the equinoxes. These differences are thought to reflect a dichotomy between the northern and southern hemispheres most probably due to difference in the solar input and associated evolutionary processes.

From month to month, we observe an evolution of the volatiles bulk composition with time. H_2O percentage decreases (with a relative increase of CO_2 and CO) during the period before the 1st equinox and similarly for the period in between equinoxes. This evolution is so far not well understood and might be linked to a H_2O reservoir not represented in our thermo-physical model. The CO_2/H_2O and CO/H_2O bulk composition ratios can locally shift up to 2 orders of magnitude. However, improvement of the correlation is still possible and might modify the bulk composition ratios.

We observe that the illuminated northern hemisphere dominates the outgassing before the 1st equinox, and the illuminated southern hemisphere dominates the outgassing in between equinoxes. The model reproduces fairly the measurement for those periods. After the 2nd equinox the northern plains are illuminated again and one would have expected to observe volatiles composition similar to the ones before the 1st equinox. Although the presence of the dust mantle at the surface is still necessary, the reproduction of ratios trend is not always satisfying our correlation criteria. In particular we see divergence close to the 2nd equinox period and for CO/H_2O density ratios. We suspect that after the 2nd equinox the outgassing pattern is influenced by contributions from both hemispheres and non-radial outgassing. Even if the southern hemisphere is no longer illuminated, the thermal inertia of the nucleus influences the outgassing of the most volatile species such as CO. We assume a similar behaviour around the 1st equinox while the activity of the nucleus move from the North towards the South to explain the discrepancies observed between the numerical results and measurements. This observation in addition to the requirement to add sometimes a desiccated dust mantle at the nucleus surface illustrates the non-negligible role played by thermal inertia on the outgassing pattern. This must be carefully taken into account while interpreting observations.

The internal structure of the nucleus is thought to be differentiated according to the different sublimation fronts of the species. Lateral compositional variation will be caused by variation in surface activity distribution and illumination from one area to another and even be enhanced by the complex shape of the nucleus.

1017 The erosion rates are calculated for specific assumptions and are likely to be overestimated
1018 (due to the global H_2O overproduction with the thermos-physical model) compared to the
1019 observations, especially for the southern hemisphere. Values must be considered as an upper limit.
1020 Sublimation and re-condensation of the gases causes porosity heterogeneities in the nucleus
1021 and the creation of a "harder" layer close to the nucleus surface which was observed by the lander
1022 Philae.
1023
1024 In order to improve our chemical and physical constraints on 67P/C-G's nucleus, further
1025 investigations need to be performed. In particular, additional free parameters can be varied to study
1026 their influence on the outgassing pattern. For instance, the investigation of the influence of the dust
1027 properties and content, porosity, thermal inertia or the ice phases (clathrate and amorphous). The
1028 absolute volatiles production curves might be improved by better take into account the input energy of
1029 a given area and the fraction of exposed volatiles at the nucleus surface. This model can also be
1030 applied to study the composition of other comets. Hence, we are in effect calibrating the model against
1031 67P/C-G to improve our understanding of what remains a complex tool.
1032
1033 Acknowledgements
1034
1035 The team from the University of Bern is supported through the Swiss National Science Foundation
1036 and through the NCCR PlanetS. The project has also received funding from the European Union's
1037 Horizon 2020 research and innovation program under grant agreement No 686709. This work was
1038 supported by the Swiss State Secretariat for Education, Research and Innovation (SERI) under
1039 contract number 16.0008-2. The opinions expressed and arguments employed herein do not
1040 necessarily reflect the official views of the Swiss Government. All ROSINA data are the work of the
1041 international ROSINA team (scientists, engineers and technicians from Switzerland, France, Germany,
1042 Belgium and the US) over the past 25 years, which we herewith gratefully acknowledge. Rosetta is an
1043 ESA mission with contributions from its member states and NASA. All data is publicly available

thanks to the ESA Planetary Science Archive. Raphael Marschall acknowledges the support from the Swiss National Science Foundation grant 184482. Olivier Mousis acknowledges support from CNES.

References

Accomazzo, A. et al. (2017). The final year of the Rosetta mission. Acta Astronautica, 136, 354-359.

A'Hearn, M. F. et al., (2011). EPOXI at comet Hartley 2. Science, 332, 1396-1400.

Attree, N. et al., (2017). Tensile strength of 67P/Churyumov-Gerasimenko nucleus material from overhangs. A&A, 611, A33.

Auger, A. T. et al. (2018). Meter-scale thermal contraction crack polygons on the nucleus of comet 67P/Churyumov-Gerasimenko. Icarus, 301, 173-188.

Balsiger, H. et al., (2007). Rosina – Rosetta orbiter spectrometer for ion and neutral analysis. Space Science Reviews, 128(1-4), 745-801.

Bardyn, A. et al., (2017). Carbon-rich dust in comet 67P/Churyumov-Gerasimenko measured by COSIMA/*Rosetta*. MNRAS, 469, S712-S722.

Biver, N. et al. (2019). Long-term monitoring of the outgassing and composition of comet 67P/Churyumov-Gerasimenko with the Rosetta/MIRO instrument. A&A, 630, A19.

Bockelée-Morvan, D. et al. (2015). First observations of H2O and CO2 vapor in comet 67P/Churyumov-Gerasimenko made by VIRTIS onboard Rosetta, A&A, 583, A6.

Bockelée-Morvan, D. et al. (2016). Evolution of CO2, CH4, and OCS abundances relative to H2O in the coma of comet 67P around perihelion from Rosetta/VIRTIS-H observations. MNRAS, 462, S170-S183.

Boehnhardt H. et al. (2017). The Philae lander mission and science overview. Philosophical Transactions of the Royal Society A-Mathematical Physical and Engineering Sciences, 375(2097), 20160248.

Brugger, B. et al., (2016). Subsurface Characterization of 67P/Churyumov–Gerasimenko's Abydos Site. The Astrophysical Journal, 822(2).Capaccionni, F., et al., (2015). The organic-rich surface of comet 67P/Churyumov-Gerasimenko as seen by VIRTIS/Rosetta. Science, 347(6220).

Capria, M. T., et al. (2017). How pristine is the interior of the comet 67P/Churyumov-Gerasimenko. MNRAS, 469, S685-S694.

Combi, M., et al. (2020). The surface distributions of the production of the major volatile species, H_2O, CO_2, CO and O_2, from the nucleus of comet 67P/Churyumov-Gerasimenko throughout the Rosetta Mission as measured by the ROSINA double focusing mass spectrometer. Icarus, 335, 113421. doi: 10.1016/j.icarus.2019.113421.

Choukroun, M. et al., (2020). Dust-to-gas and refractory-to-ice mass ratios of comet 67P/Churyumov-Gerasimenko from Rosetta observations. Space Science Reviews, 216(3), 44.

Ciarniello, M. et al. (2015). Photometric properties of comet 67P/Churyumov-Gerasimenkofrom VIRTIS-M onboard Rosetta. A&A, 583, A31.

De Sanctis, M. C. et al., (2010). Shape and obliquity effects on the thermal evolution of the Rosetta target 67P/Churyumov–Gerasimenko cometary nucleus. Icarus, 2017, 341-358.

De Sanctis, M. C. et al., (2015). The diurnal cycle of water ice on comet 67P/Churyumov-Gerasimenko. Nature, 525(7570), 500-503.

El-Maary, M. R. et al., (2016). Regional surface morphology of comet 67P/Churyumov-Gerasimenko from Rosetta/OSIRIS images: The southern hemisphere. A&A, 593, A110.

El-Maary, M. R. et al., (2017). Surface changes on comet 67P/Churyumov-Gerasimenko suggest a more active past. Science, 355(6332), 1392-1395.

Ellsworth, K. and Schubert, G. (1983). Saturn's icy satellites – Thermal and structural models. Icarus, 54(3), 490-510.

Espinasse, S., et al., (1991). Modeling of the thermal behavior and of the chemical differentiation of cometary nuclei. Icarus, 92(2), 350-365.

Feaga, L. M. et al., (2007). Asymmetries in the distribution of H2O and CO2 in the inner coma of Comet 9P/Tempel 1 as observed by Deep Impact. Icarus, 190, 345-356.

Faega, L. M. et al., (2015). Far-UV phase dependence and surface characteristics of comet 67P/Churyumov-Gerasimenko as observed with Rosetta Alice. A&A, 583, A27.

Filacchione, G. et al., (2016). Seasonal exposure of carbon dioxide ice on the nucleus of comet 67P/Churyumov-Gerasimenko. Science, 354(6319), 1563-1566.

Filacchione, G. et al., (2016). Seasonal exposure of carbon dioxide ice on the nucleus of comet 67P/Churyumov-Gerasimenko. Science, 354(6319), 1563-1566.

1127 Filacchione, G. et al., (2020). An orbital water-ice cycle on comet 67P from colour changes. Nature,
1128 578(7793), 49-52.
1129
1130 Fink, U. et al., (2016). Investigation into the disparate origin of CO2 and H2O outgassing for Comet
1131 67/P. Icarus, 277, 78-97.
1132
1133 Fornasier, S. et al., (2016). Rosetta's comet 67P/Churyumov- Gerasimenko sheds its dusty mantle to
1134 reveal its icy nature. Science, 354(6319), 1566-1570.
1135
1136 Fornasier, S. et al., (2019). Surface evolution of the Anhur region on comet 67P/Churyumov-
1137 Gerasimenko from high-resolution OSIRIS images. A&A, 630, A13.
1138
1139 Fougere, F. et al., (2016). Direct Simulation Monte Carlo modelling of the major species in the coma
1140 of comet 67P/Churyumov-Gerasimenko. Monthly Notices of the Royal Astronomical Society, 462,
1141 S156-S169.
1142
1143 Fulle, M. et al. (2017). The dust-to-ices ratio in comets and Kuiper belt objects. MNRAS, 469, S45–
1144 S49. MNRAS469,S45–S49. doi:10.1093/mnras/stx983.
1145
1146 Fulle, M. et al., (2016a). Evolution of the dust size distribution of comet 67/Churyumov–Gerasimenko
1147 from 2.2 au to perihelion. The Astrophysical Journal, 821.
1148
1149 Fulle, M. et al., (2016b). Unexpected and significant findings in comet 67P/Churyumov–Gerasimenko:
1150 an interdisciplinary view. Monthly Notices of the Royal Astronomical Society, 462, S2-S8.
1151
1152 Gasc, S. et al., (2017). Change of outgassing pattern of 67P/Churyumov–Gerasimenkoduring the
1153 March 2016 equinox as seen by ROSINA. MNRAS, 469, S109-S117.
1154

1155 Greenberg, J. M., (1998). Making a comet nucleus. A&A, 330, 375-380.

1156

1157 Groussin, O., et al., (2015). Temporal morphological changes in the Imhotep region of comet
1158 67P/Churyumov-Gerasimenko. A&A, 583, A36.

1159

1160 Groussin, O. et al., (2019). The thermal, mechanical, structural, and dielectric properties of cometary
1161 nuclei after Rosetta. Space Science Reviews, 215(5), 29.

1162

1163 Guilbert-Lepoutre, A. et al. (2016). Modelling the evolution of a comet subsurface: implications for
1164 67P/Churyumov–Gerasimenko. MNRAS, 462, S146-S155.

1165

1166 Gulkis, S. et al., (2015). Subsurface properties and early activity of comet 67P/Churyumov-
1167 Gerasimenko. Science, 347, aaa0709. doi: 10.1126/science.aaa0709.

1168

1169 Hansen, K. et al., (2016). Evolution of water production of 67P/Churyumov–Gerasimenko:
1170 anempirical model and a multi-instrument study. MNRAS, 462, S491 - S506.
1171 doi:10.1093/mnras/stw2413.

1172

1173 Hässig, M. et al., (2015). Time variability and heterogeneity in the coma of 67P/Churyumov-
1174 Gerasimenko. Science, 347(6220).

1175

1176 Herique, A., et al. (2016). Cosmochemical implications of CONSERT permittivity characterizationof
1177 67P/CG. MNRAS, 462, 516-532. doi:10.1093/mnras/stx040.

1178

1179 Hoang, M. et al., (2019). Two years with comet 67P/Churyumov-Gerasimenko: H2O, CO2, and CO as
1180 seen by the ROSINA/RTOF instrument of Rosetta. A&A, 630, A33.

1181

1182 Hoang, M. et al., (2017). The heterogeneous coma of comet 67P/Churyumov-Gerasimenko as seen by
1183 ROSINA: H2O, CO2, and CO from September 2014 to February 2016. A&A, 600, A77.
1184
1185 Hu, X. et al., (2017). Seasonal erosion and restoration of the dust cover on comet 67P/Churyumov-
1186 Gerasimenko as observed by OSIRIS onboard Rosetta. A&A, 604, A114.
1187
1188 Huebner, W. F. (2002). Composition of comets: Observations and models. Earth, Moon and Planets,
1189 89, 179-195.
1190
1191 Huebner, W. F. et al., (2006). Heat and Gas Diffusion in Comet Nuclei. ISSI Scientific Report, 258p,
1192 ISSN 1608-280X.
1193
1194 Jorda, L. et al., (2016). The global shape, density and rotation of Comet 67P/Churyumov-Gerasimenko
1195 from perihelion Rosetta/OSIRIS observations. Icarus, 277, 257-278.
1196
1197 Keller, H. U. et al., (1986). First Halley Multicolour Camera imaging results from Giotto. Nature,
1198 321(6067), 320–326.
1199
1200 Keller, H. U. et al., (2015a). The changing rotation period of comet 67P/Churyumov-Gerasimenko
1201 controlled by its activity. Astronomy and Astrophysics, 579, L5.
1202
1203 Keller, H. U. et al., (2015b). Insolation, erosion, and morphology of comet 67P/Churyumov-
1204 Gerasimenko. Astronomy and Astrophysics, 583, A34.
1205
1206 Keller, H. U. et al., (2017). Seasonal mass transfer on the nucleus of comet 67P/Chuyumov–
1207 Gerasimenko. Monthly Notices of the Royal Astronomical Society, 469, S357-S371.
1208
1209 Kitamura Y. et al., (1985). A model for the hydrogen coma of a comet. Icarus, 61(2), 278-295.

Klinger, J. et al., (1996). Toward a model of cometary nuclei for engineering studies for future space missions to comets. Planetary and Space Science, 44(7), 637-653.

Klinger, J. (1999). Thermal evolution of comet nuclei. Advances in Space Research, 23(7), 1309-1318.

Knapmeyer, M. et al., (2018). Structure and elastic parameters of the near surface of Abydos site on comet 67P/Churyumov-Gerasimenko, as obtained by SESAME/CASSE listening to the MUPUS insertion phase. Icarus, 310, 165-193.

Kochan, H. et al., (1989). Crustal strength of different model comet materials. In ESA, Physics and Mechanics of Cometary Materials, 115-119.

Kofman, W. et al., (2015). Properties of the 67P/Churyumov-Gerasimenko interior revealed by CONSERT radar. Science, 349.

Kossacki, K. J. and Czwechowski, L. (2019). Local activities of comets: an indicator of a non-uniform composition. MNRAS, 490, 2050-2055.

Kossacki, K. J. (2015). Comet 67P/Churyumov-Gerasimenko: Hardening of the sub-surface layer. Icarus, 260, 464-474.

Kramer, T. et al., (2017). Seasonal changes in of the volatile density in the coma and on the surface of the comet 67P/Churyumov-Gerasimenko. MNRAS, 469, S20-S28.

Krankowsky, D. et al. (1986). In situ gas and ion measurements at comet Halley. Nature, 321(6067), 326-329.

Krause, M. et al., (2011). Thermal conductivity measurements of porous dust aggregates: I. Technique, model and first results. Icarus, 214(1), 286-296.

Langevin, Y. et al., (2016). Typology of dust particles collected by the COSIMA mass spectrometerin the inner coma of 67P/Churyumov Gerasimenko. Icarus, 271, 76-97.

Läuter, M. et al., (2020). The gas production of 14 species from comet 67P/Churyumov–Gerasimenko based on DFMS/COPS data from 2014 to 2016. MNRAS, 498, 3995-4004. doi:10.1093/mnras/staa2643.

Läuter, M. et al., (2019). Surface localization of gas sources on comet67P/Churyumov–Gerasimenko based on DFMS/COPS data. MNRAS, 483, 852-861.

Le Roy, L. et al., (2015). Inventory of the volatiles on comet 67P/Churyumov-Gerasimenko from Rosetta/ROSINA. Astronomy and Astrophysics, A1, 12.

Maquet, L. (2015). The recent dynamical history of comet 67P/Churyumov-Gerasimenko. Astronomy and Astrophysics, 579, A78.

Marboeuf, U. (2008). Evolution physico-chimique des objets transneptuniens. PhD Thesis, Université de Franche-Comté.

Marboeuf, U. et al., (2008). Composition of Ices in Low-Mass Extrasolar Planets. The Astrophysical Journal, 681(2), 1624-1630.

Marboeuf, U. et al., (2012). A cometary nucleus model taking into account all phase changes of water ice: amorphous, crystalline, and clathrate. Astronomy and Astrophysics, 542.

Marschall, R. et al., (2020a). The Dust-to-Gas ratio, size distribution, and dust fall-back fraction of Comet 67P/Churyumov-Gerasimenko: Inferences From Linking the Optical and Dynamical Properties of the Inner Comae. Frontiers in Physics, 8, 227. doi: 10.3389/fphy.2020.00227.

Marschall, R. et al., (2020b). Limitations in the determination of surface emission distributions on comets through modelling of observational data - A case study based on Rosetta observations. Icarus, 346, 113742. doi: 10.1016/j.icarus.2020.113742.

Marschall, R. et al., (2017). Cliffs versus plains: Can ROSINA/COPS and OSIRIS data of comet 67P/Churyumov-Gerasimenko in autumn 2014 constrain inhomogeneous outgassing? Astronomy and Astrophysics, 605, A112.

Marshall, D. et al., (2017). Spatially resolved evolution of the local H2O production rates of comet 67P/Churyumov-Gerasimenko from the MIRO instrument on Rosetta. A&A, 607, A87. doi: 10.1051/0004-6361/201730502.

Massironi, M. et al., (2015). Two independent and primitive envelopes of the bilobate nucleus of comet 67P. Nature, 526, 402-405.

McDonnell, J.A.M. et al., (1986). Dust density and mass distribution near Comet Halley from Giotto observations. Nature, 321, 338-341.

Merouane, S. et al. (2017). Evolution of the physical properties of dust and cometary dust activity from 67P/Churyumov–Gerasimenko measured *in situ* by Rosetta/COSIMA. MNRAS, 469, 459-474.

Mottola, S. et al., (2014). The rotation state of 67P/Churyumov-Gerasimenko from approach observations with the OSIRIS cameras on Rosetta. Astronomy and Astrophysics, 569, L2.

Mousis, O., et al., (2018). Noble Gas Abundance Ratios Indicate the Agglomeration of 67P/Churyumov-Gerasimenko from Warmed-up Ice. The Astrophysical Journal 865. doi:10.3847/2041-8213/aadf89

Mousis, O., et al., (2015). Pits formation from volatile outgassing on 67P/Churyumov–Gerasimenko. The Astrophysical Journal, 814(1), L5.

Mumma, M. J., et al., (1987). The ortho-para ratio of water vapor in comet P/Halley. A&A, 187, 419-424.

Pätzold, M., et al., (2019). The Nucleus of comet 67P/Churyumov-Gerasimenko - Part I: The global view - nucleus mass, mass-loss, porosity, and implications. MNRAS, 483, 2337-2346. doi: 10.1093/mnras/sty3171.

Pätzold, M., et al., (2016). A homogeneous nucleus for comet 67P/Churyumov–Gerasimenko from its gravity field. Nature, 530, 63-65.

Poch, O. et al., (2016). Sublimation of water ice mixed with silicates and tholins: Evolution of surface texture and reflectance spectra, with implication for comets. Icarus, 267, 154-173.

Pommerol, A. et al., (2015). OSIRIS observation of meter-sized exposures of H2O ice the surface of 67P/Churyumov-Gerasimenko and interpretation using laboratory experiments. A&A, 583, A25.

Preusker, F. et al., (2015). Shape model, reference system definition, and cartographic mapping standards for comet 67P/Churyumov-Gerasimenko – Stereo-photogrammetric analysis of Rosetta/OSIRIS image data. Astronomy and Astrophysics, 583, A33.

1322 Prialnik, D. et al., (2004). Modeling the structure and activity of comet nuclei. Comets II, 359-387.
1323
1324 Quirico, E. et al., (2016). Refractory and semi-volatile organics at the surface of comet
1325 67P/Churyumov-Gerasimenko: Insights from the VIRTIS/Rosetta imaging spectrometer. Icarus, 272,
1326 32-47.
1327
1328 Rickman, H. et al., (1990). Formation of stable dust mantles on short-period comet nuclei. Astronomy
1329 and Astrophysics, 237, 524-535.
1330
1331 Rotundi, A. et al., (2015). Dust measurements in the coma of comet 67P/Churyumov-Gerasimenko
1332 inbound to the Sun. Science, 347(6220).
1333
1334 Rubin, M. et al., (2019). Elemental and molecular abundances in comet 67P/Churyumov-
1335 Gerasimenko. MNRAS, 489, 594-607.
1336
1337 Schroeder, I. R. H. G. et al., (2019). A comparison between the two lobes of comet 67P/Churyumov–
1338 Gerasimenko based on D/H ratios in H2O measured with the Rosetta/ROSINA DFMS. MNRAS, 489,
1339 4734-4740.
1340
1341 Sekanina, Z. (1981). Rotation and precession of cometary nuclei. Annual Review of Earth and
1342 Planetary Sciences, 9, 113-145.
1343
1344 Schoonenberg, D., and Ormel, C. W. (2017). ‘Planetesimal Formation near the Snowline: In or Out?’
1345 Astronomy & Astrophysics 602, A21. doi:10.1051/0004-6361/201630013.
1346
1347 Sierks, H. et al., (2015). On the nucleus structure and activity of comet 67P/Churyumov-Gerasimenko.
1348 Science, 347(6220), aaa1044.
1349

1350 Shinnaka, Y. et al., (2017). Imaging observations of the hydrogen coma of comet 67P/Churyumov-
1351 gerasimenko in 2015 September by the Procyon/Laica. Astronomical Journal, 153, 79. doi:
1352 10.3847/1538-3881/153/2/76
1353
1354 Spohn, T. et al., (2015). Thermal and mechanical properties of the near-surface layers of comet
1355 67P/Churyumov-Gerasimenko. Science, 349(6247), aab0464-1.
1356
1357 Taylor, M. G. G. T. et al., (2017). The Rosetta mission orbiter science overview: the comet phase.
1358 Philosophical Transactions A, 375(2097), 20160262.
1359
1360 Thomas, N. et al., (2015a). The morphological diversity of comet 67P/Churyumov-Gerasimenko.
1361 Science, 347(6220).
1362
1363 Thomas, N. et al., (2015b). Redistribution of particles across the nucleus of comet 67P/Churyumov-
1364 Gerasimenko. Astronomy & Astrophysics, 583, A17.
1365
1366 Vincent, J. B. (2015). Large heterogeneities in comet 67P as revealed by active pits from sinkhole
1367 collapse. Nature, 523(7558), 63-66.
1368
1369 Yamamoto, T. (1985). Formation environment of cometary nuclei in the primordial solar nebula.
1370 Astronomy & Astrophysics, 142, 31-36.

- ROSINA/DFMS measurements are mostly reproduced with a 1D thermo-physical comet model
- Link between ices bulk composition in the nucleus and volatiles abundance in the coma
- Volatiles outgassing of comet 67P are mainly insolation-driven due to the obliquity
- Results highlight a dichotomy in composition between the North and South hemispheres
- We provide bulk volatiles (H_2O, CO_2 and CO) composition of the comet 67P
- Dust mantle at the surface of cometary nucleus influence the volatiles outgassing

Declaration of interests

☒ The authors declare that they have no known competing financial interests or personal relationships that could have appeared to influence the work reported in this paper.

☐The authors declare the following financial interests/personal relationships which may be considered as potential competing interests: